CHALMERS
UNIVERSITY OF TECHNOLOGY

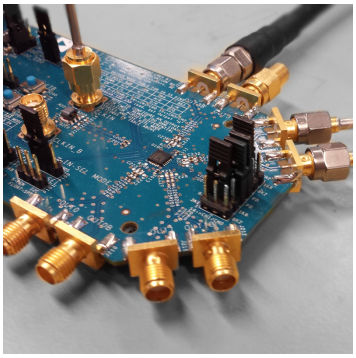
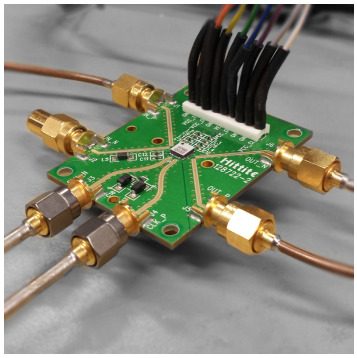
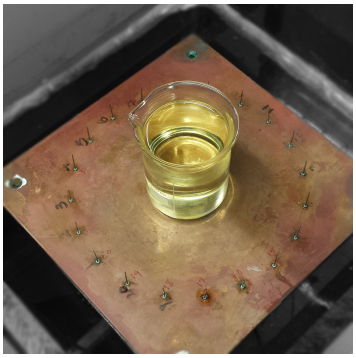
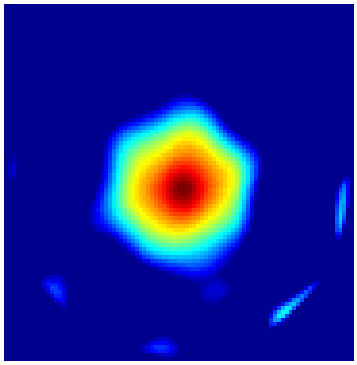

Improvement of an UWB Time Domain System for Medical Diagnostics

Master's Thesis in Biomedical Engineering

ALBERT MONTEITH

Department of Signals and Systems
CHALMERS UNIVERSITY OF TECHNOLOGY
Gothenburg, Sweden 2015

Master's thesis EX043/2015

Improvement of an UWB Time Domain System for Medical Diagnostics

ALBERT MONTEITH

CHALMERS
UNIVERSITY OF TECHNOLOGY

Department of Signals and Systems
Biomedical Electromagnetics Research Group
Chalmers University of Technology
Gothenburg, Sweden 2015

Improvement of an UWB Time Domain System for Medical Diagnostics
ALBERT MONTEITH

Supervisor: Xuezhi Zeng, Department of Signals and Systems
Examiner: Andreas Fhager, Department of Signals and Systems

Master's Thesis EX043/2015
Department of Signals and Systems
Biomedical Electromagnetics Research Group
Chalmers University of Technology
SE-412 96 Gothenburg
Telephone +46 31 772 1000

Cover: The clock distributor (top left), track-and-hold (top right), antenna array with a cylinder filled with oil (bottom left) and a reconstructed microwave tomography image of the electrical permittivity using measurements from the system described in this thesis (bottom right).

Typeset in LaTeX
Gothenburg, Sweden 2015

Improvement of an UWB Time Domain System for Medical Diagnostics
ALBERT MONTEITH
Master's Thesis in Signals and Systems
Department of Signals and Systems
Chalmers University of Technology

Abstract

The existence of contrasts in the electrical properties of healthy tissues, cancerous tissues and blood at microwave frequencies have motivated the use of ultra-wideband (UWB) diagnostic methods. Previously developed methods for UWB microwave tomography for breast cancer detection and UWB measurements for stroke detection rely on the use of a vector network analyser (VNA). This high cost, heavy, bulky and slow instrument is not ideal for clinical use and is not suitable for use in an ambulance where this technology can have the greatest impact. An UWB time domain system has previously been developed at Chalmers University of Technology with the aim of replacing the VNA with a fast, compact and low-cost system performing UWB measurements in the time domain with sufficient accuracy. This system used short pulses to perform UWB measurements and its imaging functionality was verified by imaging tests, but there are still several problems that need to be solved in order to obtain an effective imaging system.

The aim of this project was to improve the performance of the previously developed prototype. In this work, a new clock generation system was implemented, which consequently gave a higher measurement accuracy, minimized the hardware and allowed for more flexible measurements. Both pulse trains and M-sequences were considered as stimulus signals. Simulations and measurements were carried out in order to investigate the measurement accuracy for both cases.

It was found that a signal-to-noise ratio (SNR) of at least 44 dB was achieved up to 4 GHz, which is an improvement of 8 dB at 4 GHz and up to 26 dB at lower frequencies compared to that of the previous prototype. It was also shown that the use of an M-sequence as a stimulus signal results in an SNR up to 25 dB higher than that of a pulse-train based system when the noise due to jitter is negligible. Imaging tests were successfully performed using the system but it was found that the image reconstruction quality was not significantly affected by the choice of stimulus signal or measurement accuracy. The complete measurement took approximately 2.5 minutes, which is approximately half the time taken for a VNA based system.

Keywords: equivalent-time sampling, ultra-wideband (UWB), microwave tomography, M-sequence.

Acknowledgements

This thesis is a continuation of work spanning more than a decade at Chalmers University of Technology and it would be impossible without the previous work done at the Biomedical Electromagnetics research group. A great thanks goes to my supervisor Xuezhi Zeng for her friendly guidance, giving me the opportunity to work in a world-class laboratory, thorough review of my work and most of all, trust. I would also like to thank my examiner Andreas Fhager for performing the image reconstructions and purchasing the components for this system, without which this work would only be an idea on paper. Also a great thanks to Masoud for offering a strong helping hand and facing the challenges of the past year alongside me.

My greatest gratitude however goes to my family who have supported me throughout my studies and their hard work that has given me the opportunity to end up doing what I love.

Albert Monteith, Gothenburg, May 2015

Contents

1
Introduction

1.1 Medical diagnostics using microwaves

At microwave frequencies, significant contrasts exist between the electrical properties of normal tissues, cancerous tissues and blood [8, 11]. This opens up the possibility for non-invasive diagnostic systems for stroke and cancer detection by detecting the presence and location of scatterers of electromagnetic waves at microwave frequencies. Microwave diagnostic systems can offer various advantages over traditional X-ray based diagnostic systems such as using non-ionizing radiation, no painful breast compression, lower costs, higher accuracy and higher contrast in dense tissues. Microwave diagnostic systems can also operate much faster than MRI based diagnostic methods and can be implemented as minimised, portable hardware. The applications of interest in this thesis are microwave tomography for breast cancer detection and microwave measurements for stroke detection.

The information of interest in microwave diagnostics can be either the electrical properties of the tissue under investigation as a function of space, resulting in an image, or simply the existence of a significant scatterer such as a tumour or haemorrhage. This information can be viewed as the cause of the perturbed electromagnetic field observed outside the tissue when the tissue is illuminated by some incident field. Measurements of the fields outside the tissue can therefore be used to reconstruct a tomographic image of the tissue or to make a decision about whether a tumour is haemorrhage is present.

One such algorithm which solves the inverse scattering problem to produce a tomographic image is detailed in [9], and was also used in this study. The algorithm performs a model-based nonlinear inversion, whereby the resolution is not limited by diffraction. This allows for the reconstruction of electrical properties using measured fields with significantly lower frequencies [25], easing hardware requirements. High frequency measurements result in better resolution, but electromagnetic waves are highly attenuated in human tissues above a few gigahertz. High resolution images of electrical properties can be reconstructed using the frequency response over an ultra-wideband (UWB) frequency range which provides more information about the tissue than narrowband measurements [10]. Generating and measuring electromagnetic waves within such a frequency range poses several technical challenges. The design of UWB components is challenging and they often exhibit poor noise performance, impedance mismatches and nonlinearities.

1.2 Ultra-wideband systems

In medical diagnostic applications, an UWB system aims to generate one or more stimulus signals and measure the response of a linear system over a frequency range spanning several gigahertz [13, 30]. UWB measurements can be carried out in either the frequency domain or time domain.

1.2.1 Measurement methods

In frequency domain measurements the magnitude and phase of a signal is measured. The time-domain representation can then be calculated by making use of the inverse Fourier transform. Such a measurement is typically performed by generating a stepped-frequency continuous wave, which has an extremely small instantaneous bandwidth, and then measuring the magnitude and phase of the system response. This has motivated the use of a vector network analyser (VNA) for performing UWB measurements in the frequency domain [9, 18, 26]. VNAs feature a very wide bandwidth, high dynamic range and yield accurate measurements due to stable oscillators and the use of narrowband intermediate-frequency filters for eliminating wideband noise [5]. These instruments, mainly intended for laboratory use, come at an extremely high cost and are very bulky and complex. Also, due to the use of narrowband filters, settling times are long, leading to long measurement times.

Time domain measurements aim to measure the amplitude of a received waveform as a function of time. The generated stimulus signal illuminating the tissue must have an ultra-wide instantaneous bandwidth and the system must be capable of measuring the received waveform over this frequency range. Measurement of an instantaneous ultra-wide bandwidth signal does not require any intermediate-frequency stages, reducing the system complexity and allowing for much shorter measurement times. Such a system offers the possibility of simple monolithic integration, allowing for large, parallel multiport measurements. The main problems of this measurement technique are the addition of noise due to the wide input bandwidths of UWB analogue components, sampling speed limitations of data converters and the effects of timing jitter that occur when sampling high frequency signals. The capabilities of the available technology has been the limiting factor in the progress of UWB time domain systems, but advances in high-speed communication systems and radar systems are slowly making this technology a possibility for use in medicine.

1.2.2 Trends in UWB systems

Microwave imaging systems for breast cancer detection have previously been implemented and undergone clinical testing [19, 24]. However, these systems perform frequency domain measurements using a VNA, making measurements slow and sensitive to tissue movement [25]. The trend is therefore to perform measurements in the time domain with minimized hardware.

An UWB radar system previously developed for medical diagnostics and imaging, among other applications, has produced high resolution images of breast phantoms [14]. This system was implemented as an integrated circuit and is capable

of performing the same measurements as a VNA [28]. The resolution of UWB radar imaging systems are diffraction limited and must therefore operate at higher frequencies. Another disadvantage is that the resulting images represent the reflectivity throughout the imaging domain, instead of electrical properties. However, the main technological advancements of this system are the monolithic integration of the system and the use of pseudo-noise sequences as stimulus signals. These UWB signals offer major advantages over sub-nanosecond pulses such as reduced signal amplitude requirements and easier, more flexible signal generation [29].

An UWB time-domain system prototype for medical diagnostics using short pulses as stimulus signals has previously been implemented and tested at Chalmers University of Technology [37]. The purpose of this project is to replace the VNA which is currently used for microwave tomography and stroke detection with a minimized, cost-effective device performing accurate UWB measurements in a short time. This will make the technology more suitable for widespread use in clinics and even in ambulances. Measurements from this system were performed faster than the previous VNA-based system and successfully used for reconstructing tomographic images. However, this system suffers from low measurement accuracy, mainly due to timing jitter and low transmitted power. Some subsystems were implemented as laboratory instruments which is not desired to their size and cost. This system therefore requires more work before it can undergo clinical testing and be used in clinical environments.

1.3 Thesis aim, scope and structure

The aim of the work described in this thesis was to improve the performance of the previous generation of the time domain system developed at Chalmers and to reduce the number of laboratory instruments in the system. The scope of this thesis covers the design and implementation of the hardware in the diagnostic system as a prototype consisting of off-the-shelf modules. A focus was placed on developing a theoretical understanding of the required clocking scheme to reduce jitter and identifying and minimising the sources of measurement errors in the system. A comprehensive comparison between the use of pulse trains and pseudo-noise as stimulus signals was performed in order to find out which signal yields better system performance. While there are a vast number of possible applications for this system, a focus was placed on microwave tomography for breast cancer detection.

In Chapter 2, the relevant theoretical background of the stimulus signals and sampling scheme is presented. Chapter 3 discusses the errors affecting the measurement accuracy and in Chapter 4 the implementation of the new generation of the time domain system prototype is discussed. Results characterizing the performance of the new system are presented in Chapter 5. The final chapter (Chapter 6) provides a summary of the work and some future prospects.

2
Theory

This chapter covers the theoretical background of the system. After an overview of the system is given, the stimulus signal properties and sampling strategy are discussed in detail.

2.1 Overview of system

A typical UWB time-domain system for medical imaging consist of a transmitter, antenna array, receiver and a personal computer (PC) for reconstruction. A single transmitter and receiver are used to perform measurements of the time-domain response between two ports of the antenna array via a microwave switching matrix. The transmitter is responsible for generating the UWB stimulus signal and the receiver measures the received response. The switching matrix allows for all antenna combinations to be connected to the transmitter and receiver ports. The shaded region is the object being imaged, which together with the antenna array and switching matrix forms the system under test (SUT). The measured signals are processed on a PC in order to characterize the SUT and reconstruct a tomographic image of the electrical permittivity and conductivity.

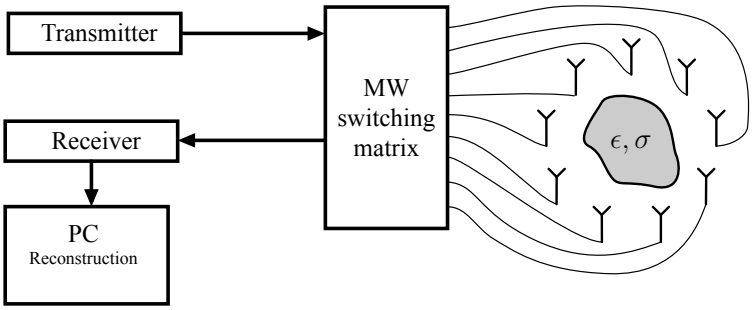

Figure 2.1: Simplified block diagram of the system.

2.2 Stimulus signal

Following linear system theory, the SUT frequency response is characterised over the frequency range that it is stimulated by. The stimulus signal should therefore have spectral components throughout the frequency range of interest and enough power such that the SUT response is sufficiently higher than noise. The SUT frequency response range of interest in this application is from a few hundred megahertz to approximately 4 GHz. This range was chosen for high image resolution, while still being capable of penetrating human tissues [34]. Above this range the penetration depth decreases significantly. The signal is also required to be periodic. The two signals that were investigated are pulse trains and pseudo-noise sequences. The stimulus signal $s(t)$ can ideally be represented as a convolution of a single period $p(t)$ and a pulse train with period $1/f_{rep}$ to make it periodic:

$$s(t) = p(t) * \sum_{n=-\infty}^{\infty} \delta\left(t - \frac{n}{f_{rep}}\right), \tag{2.1}$$

which has the Fourier transform

$$S(f) = f_{rep} \cdot \sum_{k=-\infty}^{\infty} P(kf_{rep}) \cdot \delta\left(f - kf_{rep}\right) \tag{2.2}$$

The spectrum of the transmitted signal therefore only consists of a series of Dirac delta functions separated by the repetition rate f_{rep}, which is then the frequency resolution of the characterized SUT. The signal bandwidth and power are determined by the shape of $p(t)$, which is considered next.

2.2.1 Pulse trains

For a pulse train, $p(t)$ can be modelled as a narrow Gaussian-shaped pulse for which the Fourier transform has a wide continuous Gaussian-shaped curve. The Fourier transform of a 1 V peak-to-peak Gaussian pulse train with repetition rate f_{rep} and full width at half maximum (FWHM) is

$$S(f) = \sigma\sqrt{2\pi} f_{rep} \sum_{k=-\infty}^{\infty} \exp\left[-2\left(\sigma\pi k f_{rep}\right)^2\right] \cdot \delta\left(f - kfrep\right) \tag{2.3}$$

where $\sigma = \text{FWHM}/\left(2\sqrt{2\ln 2}\right)$. The average power of the signal is then

$$P_{ave} = \int_{-\infty}^{\infty} |S(f)|^2 \, df \tag{2.4}$$

$$= 2\pi \left(\sigma f_{rep}\right)^2 \sum_{k=-\infty}^{\infty} \exp\left[-\left(2\sigma\pi k f_{rep}\right)^2\right] \tag{2.5}$$

Note that P_{ave} is directly proportional to f_{rep}^2 for a Gaussian pulse train. A high pulse repetition rate and/or a high pulse amplitude is therefore required for the signal to have a high power. This presents a trade-off between frequency resolution and SNR. For a fixed frequency resolution, the pulse amplitude must be increased

to achieve a high SNR. However, high field strengths could result in distortion due to nonlinearities in the system and even damage to tissues [15]. The pulse width FWHM determines the signal bandwidth and is usually fixed, or a coarse pulse width adjustment is available [35, 38].

Sub-nanosecond rise time pulses require unconventional signal generation techniques using avalanche transistors, step-recovery diodes, tunnel diodes or non-linear transmission lines. An in-depth discussion of these techniques is treated in [2]. Repetitive pulses are triggered by a clock with a frequency equal to the repetition rate f_{rep}. Advantages of pulse generating circuits are that they can be implemented using inexpensive components, they can be designed to consume little power and some pulse generation techniques allow for easy implementation. The main drawback of pulse generators is that a large amount of energy must be compressed into a very short time in order to obtain a wide bandwidth and large SNR. Cycle-to-cycle jitter is also a limiting factor in pulse generation techniques [15, 17].

2.2.2 Pseudo-noise signals

The pseudo-noise signal that will be used in this application is the maximal-length pseudo-random binary sequence (M-sequence) with non-return-to-zero encoding. The signal $p(t)$ can be visualised to be a sequence $\{a_n\}$ of random bits where each bit is mapped to a specific voltage, eg. $a_n \in \{1, -1\}$, as shown in Figure 2.2a. These signals are easily generated using a length m shift register with linear feedback [7]. The m-length shift register cycles through all possible combinations except for the all-zero state[1], and is therefore periodic with each period consisting of $2^m - 1$ shift register clock cycles. The repetition rate is therefore $f_{rep} = f_b/(2^m - 1)$, where f_b is the clock of the M-sequence generator. The motivation for using this signal is because its energy is distributed evenly throughout its period and M-sequences are relatively easy to generate compared to other UWB signals. M-sequence generators with f_b operating in the tens of gigahertz have been implemented as monolithic microwave integrated circuits using silicon-germanium fabrication processes [20, 22, 27]. An m-length M-sequence with repetition rate f_{rep} has the Fourier transform

$$S(f) = \frac{1}{2^m - 1} \sum_{k=-\infty}^{\infty} A_k \cdot \operatorname{sinc}\left(\frac{k}{2^m - 1}\right) \cdot \delta\left(f - k f_{rep}\right) \tag{2.6}$$

where A_k is the discrete Fourier transform (DFT) of a_n. M-sequences have a sinc^2 power spectrum as shown in Figure 2.2b. The zeros of this spectrum occur at integer multiples of the clock f_b of the M-sequence generator, therefore f_b controls the signal bandwidth. The average power of the signal is then

$$P_{ave} = \frac{1}{(2^m - 1)^2} \sum_{k=-\infty}^{\infty} \left| A_k \cdot \operatorname{sinc}\left(\frac{k}{2^m - 1}\right) \right|^2 \tag{2.7}$$

Note that the above expression is independent of f_{rep}, showing that unlike a pulse train, the average power of an M-sequence is not affected by variations of the repetition rate. Approximately 80% of the signal power is in the frequency range from

[1] An all-zero state will result in all successive states to be all-zero.

DC to $f_b/2$. The frequency $f_b/2$ will therefore be considered to be the bandwidth of the signal. The output of an M-sequence generator is usually low-pass filtered to $f_b/2$ in order to avoid aliasing of the sidelobes of the sinc function and minimise the accumulation of noise due to jitter. An M-sequence generator therefore requires a clock with a frequency that is double the desired signal bandwidth.

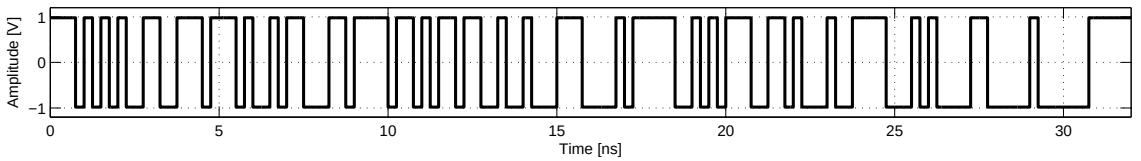

(a)

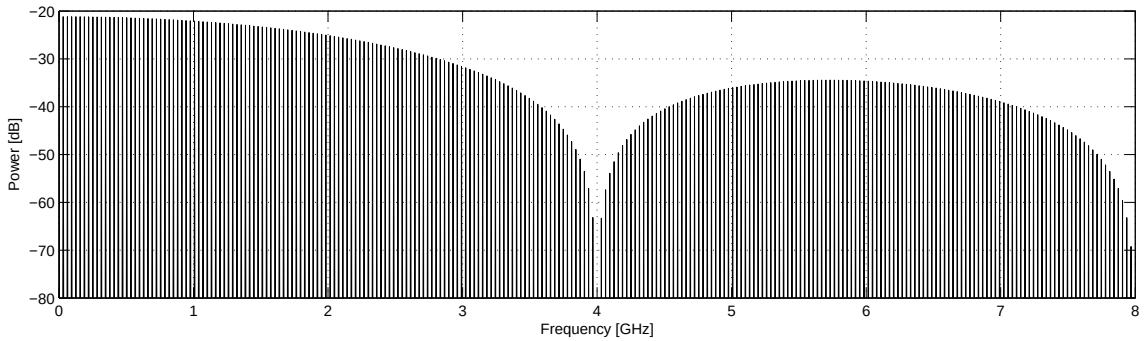

(b)

Figure 2.2: Plots of a) a single period and b) power spectrum of an m=7 M-sequence with clock rate f_b=4 GHz.

2.3 Equivalent-time sampling

Current analogue-to-digital converter (ADC) technologies are incapable of sampling an UWB signal with frequency content from DC to several gigahertz with sufficient resolution in real time. One way of circumventing this problem is by repeating the UWB signal (eg. a short pulse) to form a periodic signal with a period repetition rate of f_{rep} (which is also the fundamental frequency). Samples are then taken over several periods at a rate that is below the Nyquist rate. After a sufficient number of periods a complete period can be reconstructed from the recorded samples. This sampling strategy is known as equivalent-time sampling.

A special case of equivalent-time sampling is to take one sample per period, each time at a further position in the period than the previous sampling instant. This new implicit sampling rate f_s is therefore slightly lower than f_{rep}. After several periods a single period can be reconstructed from the samples. This strategy is illustrated in Figure 2.3. The advantages of using equivalent-time sampling are that a much slower, low cost ADC can be used and the overall system is simple since no intermediate frequency mixing stage is required and less power is consumed. This sampling approach does however come with some drawbacks and complications which will be discussed below.

2.3.1 Synchronous equivalent-time sampling

In this study, only the case where a single sample taken per period is considered. This is the optimal case for sequential sampling, i.e. this is the fastest equivalent-time sampling strategy for which the samples do not need to be reordered. In equivalent-time sampling, the equivalent-time sampling rate f_{eq} is the theoretical sampling rate for the case where all samples are taken in a single period, instead of several successive periods. The following relationship should be satisfied:

$$f_{eq} = N_s f_{rep} \tag{2.8}$$

where $N_s = 1, 2, 3, ...$ is the number of samples in the recorded period. This is desired in order to avoid spectral leakage and to preserve the phase in successive measurements. These effects are proved in Appendix A. Such a system will be termed a synchronous equivalent-time sampling system. In a synchronous equivalent-time system, an offset frequency $f_{os} = f_{rep} - f_s$ exists which has a period equal to the time required to measure a single period. A clock with this frequency can then be used to trigger the recording of samples, each time starting at the same phase of the period. This allows for coherent averaging of recorded periods within digital hardware such as a field-programmable gate array (FPGA), thereby decreasing the amount of data needed to be transmitted to a computer for reconstruction. The condition for synchronization can then also be expressed as

$$f_{rep} = (N_s + 1) f_{os} \tag{2.9}$$

$$f_s = N_s f_{os} \tag{2.10}$$

The number of signal periods that must be repeated in order to measure one period using equivalent time sampling is $N_p = N_s + 1$. Figure 2.3 shows a timing diagram illustrating this concept for $N_s = 4$, or equivalently, $N_p = 5$. As N_s increases, the equivalent sampling rate f_{eq} increases. This parameter must therefore be chosen such that the Nyquist criterion is met.

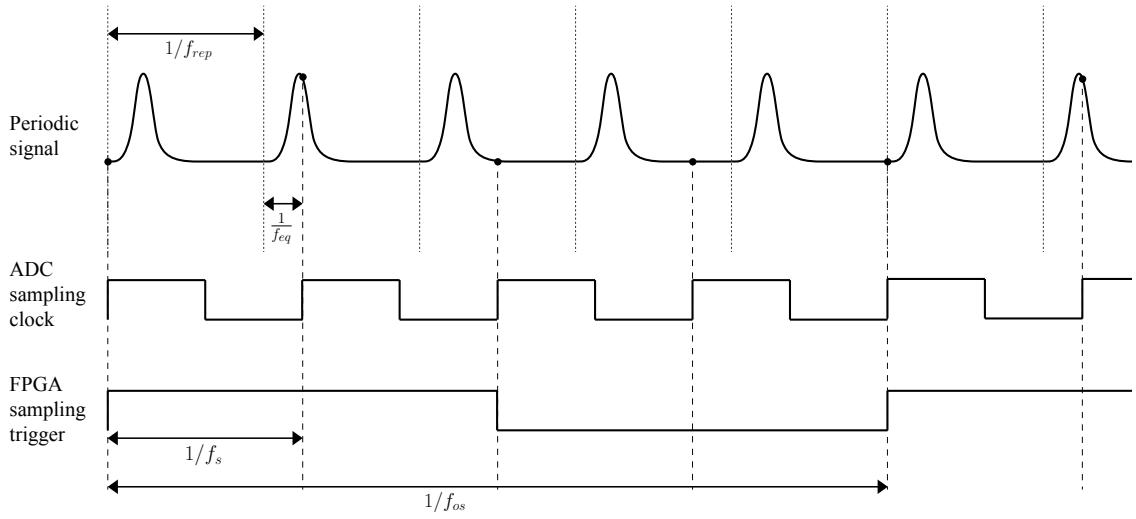

Figure 2.3: Timing diagram of a synchronous equivalent time sampling system with $N_p = 5$. Black dots in the upper signal indicate samples.

2.3.2 Frequency resolution and measurement time

For a periodic signal, the power lies at multiples of the fundamental harmonic, limiting the frequency resolution when characterizing the SUT. The repetition rate f_{rep} is the best resolution that can be obtained using equivalent-time sampling because the discrete DFT frequency resolution for a single sampled period is

$$\triangle f = \frac{f_{eq}}{N_s} = \frac{f_{eq}}{f_{eq}/f_{rep}} = f_{rep} \tag{2.11}$$

For a pulse train generator, f_{rep} can easily be varied and is independent of the bandwidth but in an M-sequence system it is dependent on the M-sequence length m and clock frequency f_b according to the relationship $f_{rep} = f_b/(2^m - 1)$. If an M-sequence is band-limited to $f_b/2$ then the number of frequency points within the bandwidth is a fixed number $(2^m - 1)/2$. These relationships are plotted in Figure 2.4. A higher shift register length m results in better frequency resolution, but an increase in m comes at a cost. For a high m, the number of samples N_s required to satisfy the Nyquist criterion becomes extremely large according to (2.8), increasing measurement times. A long shift register also results in large propagation delays, making a large m difficult to implement at high clock rates [20].

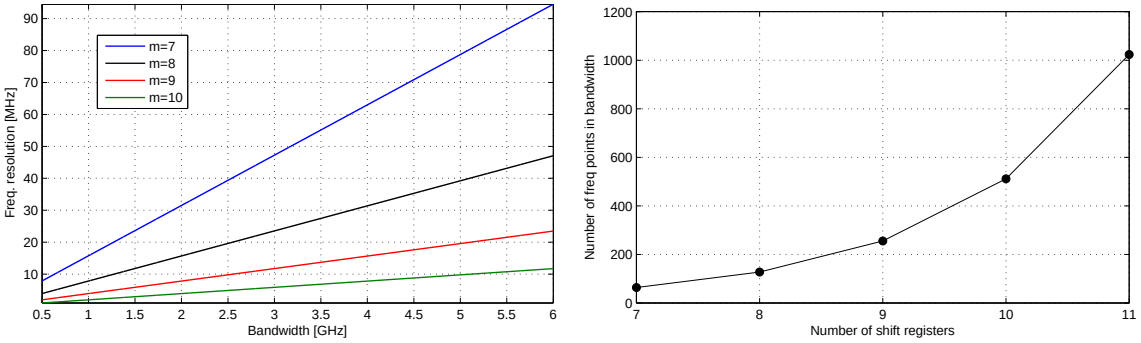

(a) **(b)**

Figure 2.4: Plots of a) the frequency resolution vs signal bandwidth and b) frequency points within the bandwidth vs m for an M-sequence.

The pulse system therefore provides greater flexibility for controlling the frequency resolution whereas a change in m is required for the M-sequence case, requiring changes in hardware. But a higher m (and lower f_{rep}) will result in the same average power (and thus SNR) for an M-sequence, whereas improving the frequency resolution for a pulse train reduces the average power. A good frequency resolution (low f_{rep}) is desired as it yields more spectral information about the SUT, but this consequently increases the measurement time ($1/f_{os}$). A trade-off must therefore be made between frequency resolution and measurement time.

3
Error analysis

In this chapter the systematic and random errors present in the system are discussed and simulation results verifying the theory are presented.

3.1 Systematic errors

Systematic errors occur due to reproducible inaccuracies in the measurement system such as distortion by components and delays by cables. Another problem which will be treated as a sytematic error is the unknown phase shift at system startup, which occurs due to unpredictable oscillator and PLL transient characteristics. The sampling clock (f_s) will therefore have an unknown phase shift relative to the repetition clock (f_{rep}). In other words, the phase of the FPGA sampling trigger in Figure 2.3 is unknown after startup. In equivalent-time sampling this can be treated as an unknown phase shift in the transmitted signal $T(f)$. Since only the received signal is measured, a calibration is required to eliminate these errors.

For the following discussion, an error network will be introduced as shown in Figure 3.1. As shown in the figure, the input reference plane is at the end of the cable leading into the SUT, with the received signal referenced at the start of the cable leaving the SUT. It is assumed that all ports are matched to 50 Ω. Subindex i is the index of the receiving antenna and j is the index of the transmitting antenna.

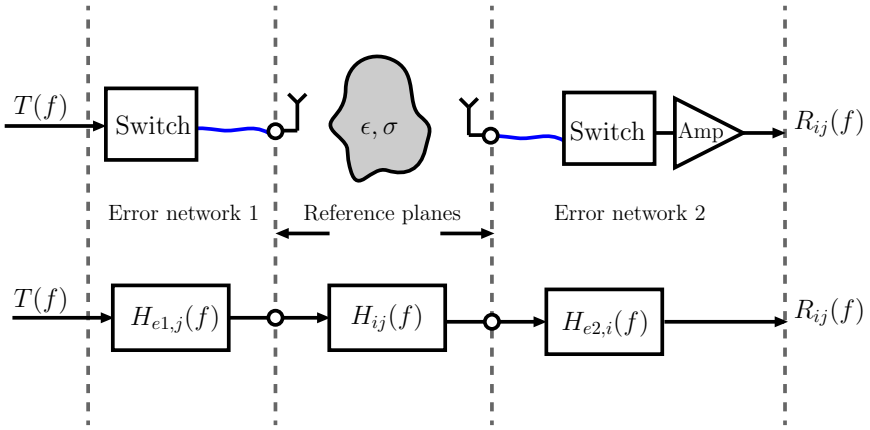

Figure 3.1: Block diagram of the measurement showing the error network and reference plane. Blue lines indicate cables.

In microwave tomography, a measurement of both a reference system[1] and a system with an object to be imaged is performed. Using the reference system, the received signal is

$$R_{ref,ij}(f) = T(f) \cdot H_{e1,j}(f) \cdot H^{meas}_{ref,ij}(f) \cdot H_{e2,i}(f) \tag{3.1}$$

and for a system with an object to be imaged the received signal is

$$R_{obj,ij}(f) = T(f) \cdot H_{e1,j}(f) \cdot H^{meas}_{obj,ij}(f) \cdot H_{e2,i}(f) \tag{3.2}$$

All systematic errors are eliminated by taking the ratio of the above two expressions and multiplying with a simulated reference system response $H^{sim}_{ref,ij}(f)$:

$$H^{cal}_{obj,ij}(f) = \frac{R_{obj,ij}(f)}{R_{ref,ij}(f)} \cdot H^{sim}_{ref,ij}(f) = \frac{H^{meas}_{obj,ij}(f)}{H^{meas}_{ref,ij}(f)} \cdot H^{sim}_{ref,ij}(f) \tag{3.3}$$

The transfer function $H^{cal}_{obj,ij}(f)$ is then used by the image reconstruction algorithm [9]. For this calibration procedure to work, the hardware must keep track of the phase of the received signal between measurements of $R_{ref,ij}$ and $R_{obj,ij}$, stressing the importance of the FPGA sampling trigger. This calibration procedure only eliminates linear systematic errors. Nonlinear systematic errors were minimised by operating components within the peak-to-peak ranges specified by their manufacturers.

3.2 Random errors

Common random errors in electronic measurement systems are thermal noise and quantization noise. The effects of phase noise becomes significant when high frequency signals are sampled. The following sections will discuss the effects of these noise sources on the SNR and present methods for measuring the performance of the system in the presence of random noise.

3.2.1 Voltage noise: Quantization and thermal noise

The measurement error due to discretized amplitudes in an ADC introduces noise into the sampled signal. The quantization noise power can be approximated to be $\sigma^2_Q = \text{LSB}/12$, where LSB is the voltage range of the least significant bit. In the applications of interest a 12 bit resolution ADC will be used, resulting in a maximum SNR of 74 dB for a full scale sinusoidal input[2]. Quantization noise can be further reduced by increasing the bits of resolution but this will not lead to a significant improvement in SNR because the other noise sources dominate in UWB receivers.

Thermal noise occurs due to the movement of charges within conductors of the sampling system, appearing as noise at the input of the sampler [16]. The thermal noise power is $\sigma^2_T = k_B T B$, where k_B is Boltzmann's constant, T the receiver

[1] In the reference system, the tissue to be imaged is not within the antenna array.

[2] The maximum theoretical SNR due to quantization noise is SNR $= 6.02N + 1.76$ [dB] for a uniform, full scale input to an N-bit quantizer.

temperature and B the receiver bandwidth, which must be at least as wide as the bandwidth of the input signal (4 GHz). The SNR due to voltage noise will therefore be dominated by the SNR due to thermal noise[3] because of the large input bandwidth required.

The voltage noise does not depend on the power of the input signal, therefore the SNR due to voltage noise for an M-sequence system will be higher than for a pulse train system simply because a higher input signal power is possible for the same peak-to-peak input range of the receiver.

3.2.2 Phase noise and timing jitter

For a non-ideal sinusoidal sampling clock signal, the signal may be represented as $A\sin[2\pi f_s + \theta_{PN}(t)]$, where A is the amplitude and $\theta_{PN}(t)$ is a random phase noise component. In an ADC, a sampling clock with phase noise has the effect of not sampling the input signal at the ideal sampling instants. The n^{th} sample of an ADC input signal $x(t)$ can therefore be expressed as

$$x_s(n) = x(nT_s + \delta_J(n)) \tag{3.4}$$

where $T_s = 1/f_s$ and $\delta_J(n)$ is a random variable with a Gaussian distribution and is known as timing jitter. The timing jitter discussed here will be considered to be the total root mean square (RMS) jitter σ_J in the system and is assumed to have a normal distribution with zero mean and variance σ_J^2. Taking the first order Taylor expansion of $x_s(n)$ around nT_s we obtain [33]

$$\begin{aligned} x_s(n) &\approx x(nT_s) + x'(nT_s)\delta_J \\ &= x(nT_s) + \varepsilon_J(n) \end{aligned} \tag{3.5}$$

where $x(nT_s)$ is the sampled signal in the absence of jitter and $\varepsilon_J(n)$ is the error voltage due to jitter. Figure 3.2 illustrates (3.5) graphically. Note that the relationship between the jitter $\delta_J(n)$ and the error $\varepsilon_J(n)$ is non-linear and is highly dependent on the shape of the signal being sampled. This is a valid approximation if the jitter is small compared to the rate of change of the signal[4]. This error voltage is therefore a random variable resulting in wideband noise.

[3]This parameter can be found in the ADC datasheet as the SNR with the lowest input frequency, where timing jitter has a negligible influence on performance.

[4]This inequality is derived by assuming that the 3rd Taylor series term is much smaller than the 2nd term, giving $\delta_J(n) \ll 2x'(nT_s)/x''(nT_s)$.

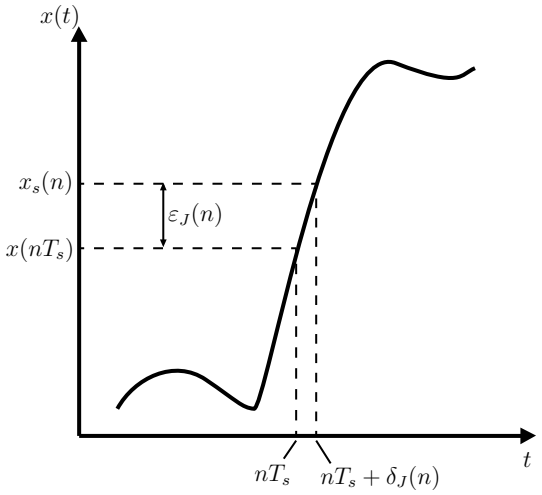

Figure 3.2: Illustration of how timing jitter introduces noise into a sampled signal.

The only frequencies of interest are $f = kf_{rep}$ where $k = 0, 1, 2, ...$ because signal power only lies at these frequencies. If it is assumed that the jitter is uncorrelated with the sampled waveform, the sampling process in the presence of jitter does not add or remove power [31]. This can be modelled as a jitter adding subsystem within the ADC as shown in Figure 3.3. A portion of the ideally sampled signal power therefore gets converted into noise power and the signal power component P_{sig} after sampling in the presence of jitter is less than the input signal power P_{in}. This can be written as

$$P_{in}(k) = P_{out}(k) = P_{sig}(k) + P_J(k) \tag{3.6}$$

where $P_{in}(k)$ and $P_{out}(k)$ are the jitter subsystem input and output signal powers at the frequency $f = kf_{rep}$ and $P_J(k)$ is the wideband noise power due to the input at $f = kf_{rep}$. This equation implies that in the presence of jitter, the signal power at the harmonics $k = 1, 2, 3, ...$ is reduced and the power lost is turned into additive wideband noise, raising the noise floor. The jitter adding subsystem is therefore a nonlinear system.

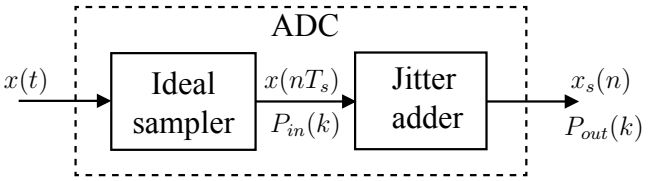

Figure 3.3: Digram of how jitter is modelled in an ADC.

Once the ADC input signal has reached a periodic steady state, it can be represented as a Fourier series:

$$x_s(nT_s) = \frac{a_0}{2} + \sum_{k=1}^{\infty} [a_k \cos(2\pi k f_{rep} n T_s) + b_k \sin(2\pi k f_{rep} n T_s)] \tag{3.7}$$

The Fourier coefficients can be obtained from the FFT of the ideal input signal. The total additive wideband noise power contributed to by all signal harmonics is then [23]

$$P_{\varepsilon_J} = E\left[x'(nT_s)^2 \cdot \delta_J^2\right] \tag{3.8}$$

$$= \frac{1}{2}\sum_{k=1}^{\infty}\left[(a_k^2 + b_k^2)(2\pi k f_{rep}\sigma_J)^2\right] \tag{3.9}$$

The signal power terms in (3.6) can then be calculated as follows

$$P_{in}(k) = \frac{a_k^2 + b_k^2}{2} \tag{3.10}$$

$$P_{sig}(k) = P_{in}(k) - P_J(k) \tag{3.11}$$

where

$$P_J(k) = \frac{1}{2}(a_k^2 + b_k^2)(2\pi k f_{rep}\sigma_J)^2 \tag{3.12}$$

is the jitter noise power contributed to by the kth harmonic of the sampled signal and shows that the higher the frequency content of a sampled signal, the greater the added noise due to jitter. The dependence on the squared magnitude $(a_k^2 + b_k^2)$ indicates that a higher signal power results in more noise due to jitter. Therefore the performance of this system, which operates up to several gigahertz, is limited by the effects of jitter.

This model was derived for jitter that has a Gaussian distribution and (3.9) is only valid if the noise due to jitter is white noise. This model is therefore only useful for gaining an understanding of the effects of jitter. In most cases, much of the phase noise power is distributed close to the center frequency of the clock signal, known as in-band phase noise, as shown in Figure 3.4. Spurs may also be present[5]. When sampling with such a clock, this phase noise spectrum convolves with the signal being sampled, widening the Dirac delta functions in the case of periodic signals. In equivalent-time sampling, the phase noise spectrum is also widened by a factor of $N_p = N_s + 1$ due to the abscissa scaling from the apparent sampling rate f_s to the equivalent sampling rate f_{eq}. To conserve power, the phase noise power per frequency unit decreases by a factor N_p. This should be kept in mind when selecting N_s and/or f_{rep} because narrow spacings between signal harmonics can result in significant in-band phase noise spectra overlapping and reducing the SNR.

[5]Noise concentrated at a single frequency is known as a spur and appears as a spike in the frequency domain.

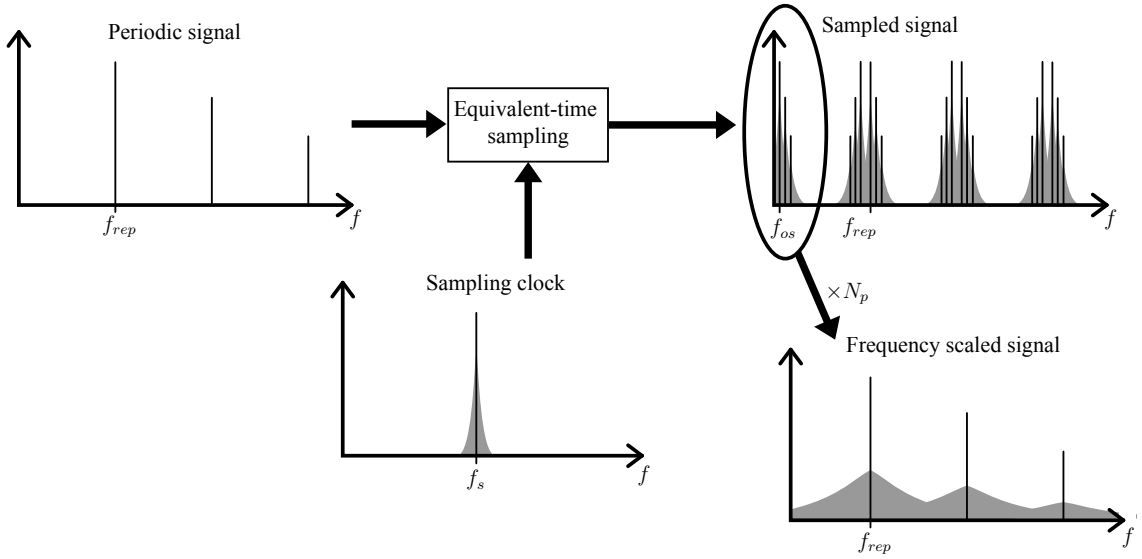

Figure 3.4: Illustration of how the in-band phase noise spectrum on the sampling clock affects the spectrum of an equivalent-time sampled signal.

3.2.3 Estimating the SNR from measurements

If N_m measurements of the sampled signal $y(n)$ are taken, the estimate of the SNR at each frequency $f = kf_{rep}$ is defined as

$$\mathrm{SNR}_{\mathrm{dB}}(k) = 10\log_{10}\left(\frac{\overline{|Y(k)|}^2}{\sigma^2_{noise}(k)}\right) \tag{3.13}$$

where $\overline{|Y(k)|}$ is simply the average of the fast Fourier transform (FFT) magnitude of all N_m measurements and $\sigma^2_{noise}(k)$ is the noise power, calculated as the variance of the magnitude spectrum [6]:

$$\sigma_{noise}(k) = \frac{1}{N_m}\sum_{i=1}^{N_m}\left(|Y_i(k)| - \overline{|Y_i(k)|}\right)^2 \tag{3.14}$$

In some cases, the total SNR is of interest and is calculated as

$$\mathrm{SNR}_{\mathrm{Tot,\ dB}} = 10\log_{10}\left[\frac{\sum_{k=1}^{N_h}\overline{|Y(k)|}^2}{\sum_{k=1}^{N_h}\sigma^2_{noise}(k)}\right] \tag{3.15}$$

where N_h is the number of signal harmonics that are of interest. In this study, N_h was chosen to be the number of harmonics within the signal bandwidth.

3.2.4 Theoretical estimate of the SNR

Let the n^{th} sample of the sampled signal $y(n)$ be expressed as

$$\begin{aligned} y(n) &= x(nT_s + \delta_J(n)) + \varepsilon_T(n) + \varepsilon_Q(n) \\ &\approx x(nT_s) + \varepsilon_J(n) + \varepsilon_T(n) + \varepsilon_Q(n) \end{aligned} \tag{3.16}$$

where $x(nT_s)$ is the signal in the absence of noise, $\varepsilon_J(n)$ the noise due to jitter, $\varepsilon_T(n)$ the thermal noise and $\varepsilon_Q(n)$ the quantization noise. The theoretical estimate of the SNR(k) is defined as

$$\mathrm{SNR}_{\mathrm{dB}}(k) = 10\log_{10}\left(\frac{P_{sig}(k)}{\sigma^2_{noise}(k)}\right) \tag{3.17}$$

If all noise sources are assumed to be white and uncorrelated, $\sigma^2_{noise}(k)$ can be estimated as

$$\sigma^2_{noise}(k) = \frac{\left(P_{\varepsilon_J} + \sigma^2_T + \sigma^2_Q\right)}{N_s \cdot N_{ave}} \tag{3.18}$$

where N_{ave} is the number of coherent averages taken. The division by N_s (the FFT length) occurs because the noise power (assumed to be distributed evenly in the frequency domain) is divided equally into each FFT bin. This is equivalent to the FFT processing gain [16] and is included here because the FFT is part of the signal chain prior to image reconstruction. This model of the SNR due to jitter explains two common observations: jitter has a low-pass effect after averaging ($P_{sig}(k)$ decreases with frequency) and the noise floor increases with added jitter (the noise is wideband).

3.3 Simulation results

The purpose of the simulation was to determine the SNR at different frequencies for the pulse and M-sequence systems under different noise and system parameters. Figure 3.5 shows a simplified block diagram of the simulated system. This system simulates a pulse and M-sequence system using a signal bandwidth of 4 GHz and a receiver consisting of a 12-bit ADC and wideband (5 GHz) track-and-hold (T&H), taking all three random noise sources described into account. Timing jitter was assumed to have a normal distribution with zero mean. Table 3.1 shows the receiver parameters used in the simulation, unless otherwise stated. The simulation was performed with the SUT as an ideal cable, a system that just attenuates the input signal and finally using a real system transfer function. The system transfer function used was that between two antennas of the antenna array used in [37], characterized using a VNA. The method used for performing time domain simulations using the S-Parameters measured by the VNA is described in Appendix B.

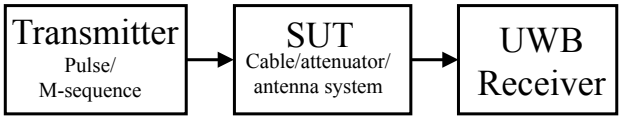

Figure 3.5: Simplified block diagram of the simulated system.

Parameter	Value
T&H full scale range V_{pp}	1 V
T&H RMS thermal noise σ_T	394 μV
ADC RMS thermal noise σ_T	172 μV
T&H RMS aperture jitter $\sigma_{J,A}$	30 fs RMS
RMS Clock jitter $\sigma_{J,CLK}$	1.5 ps RMS

Table 3.1: Receiver parameters used in the simulation.

3.3.1 Effect of timing jitter on the SNR

As mentioned in the previous section, the noise power due to jitter is dependent on the signal shape. The SNR, computed using (3.13), was compared for systems with a pulse train and M-sequence as the stimulus signals. The transmitter was directly connected to the receiver in this simulation. The results shown in Figure 3.6 show that the SNR is higher when using an M-sequence, but this advantage is only significant at a low level of jitter. For the M-sequence, the SNR predicted by the model in (3.17) is also shown and agrees well with the simulated result. The predicted SNR is not shown for the pulse train case because it did not agree well with the simulated results. This is because the noise due to jitter for a pulse train is not white noise and therefore the model in (3.17) is not valid. Due to the random nature of an M-sequence, the noise due to jitter is approximately white and therefore the model agrees well with the simulated results.

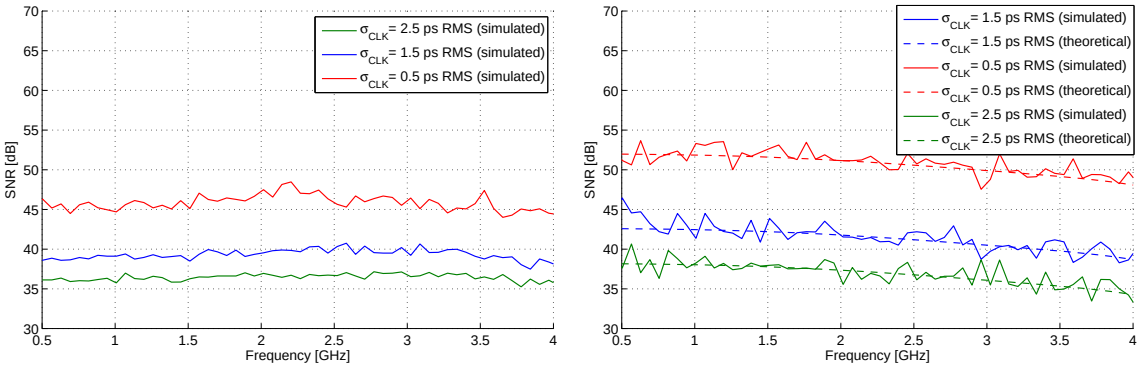

(a) Pulse train **(b)** M-sequence (m=7, f_b=8 GHz)

Figure 3.6: Comparison of the SNR for different amounts of timing jitter.

3.3.2 Effect of repetition rate on the SNR

As predicted by (2.5) and (2.7), a change in repetition rate results in a decrease in signal power for a pulse train, while the power of an M-sequence remains unaffected. The simulation results testing this theory are showed in Figure 3.7. By halving the repetition rate f_{rep}, the SNR of a system using a pulse train drops by 6 dB, while the SNR of an M-sequence system is unaffected.

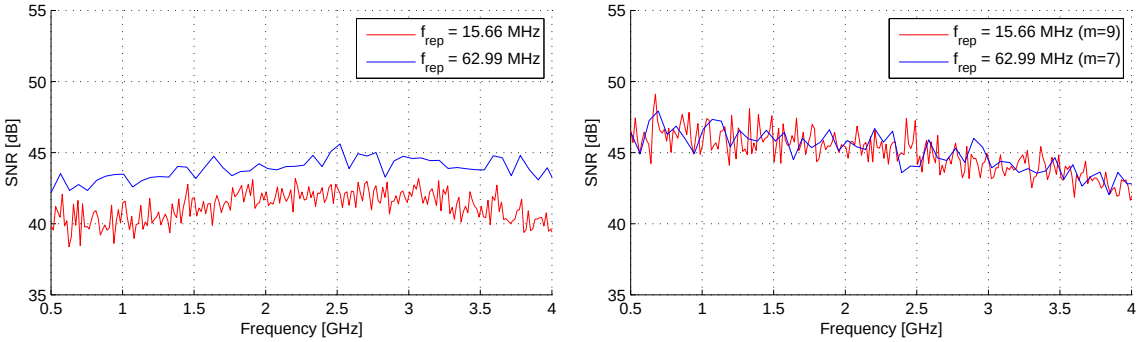

(a) Pulse train **(b)** M-sequence (m=7, f_b=8 GHz)

Figure 3.7: Comparison of the SNR for different period repetition rates f_{rep}.

3.3.3 Effect of attenuation on the SNR

The model of noise due to jitter presented in the previous section predicts that lower signal amplitudes will reduce the noise due to jitter. However this also causes a decrease in signal power. Figure 3.8 shows how the SNR is affected for both a pulse train and M-sequence system when the signal is attenuated between the transmitter and receiver. In the presence of jitter the SNR of a pulse train is decreased more than for an M-sequence at high levels of attenuation. This is because the SNR of an M-sequence is limited by noise due to jitter, not low signal power as is the case for the pulse train. The SNR of the M-sequence is limited by noise due to jitter for an attenuation of up to 20 dB, beyond which the signal power is so low that the effects of jitter become negligible. For an attenuation of 30 dB an M-sequence yields significantly better system performance, indicating that the M-sequence is more suitable for low power systems.

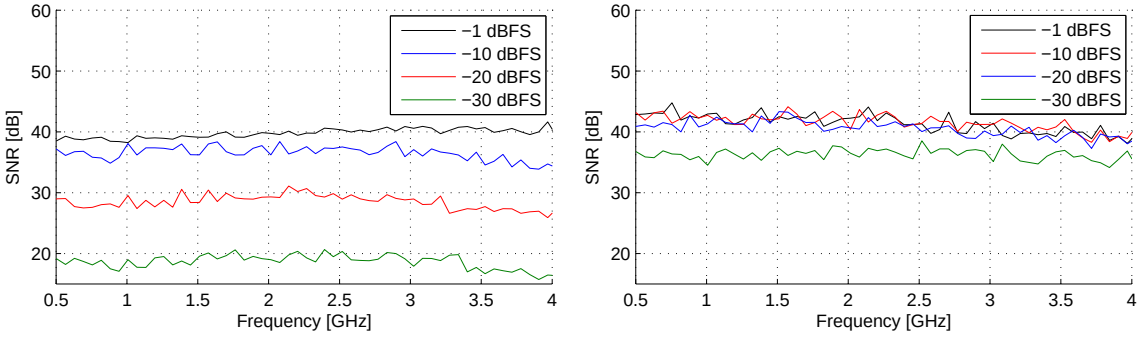

(a) Pulse train **(b)** M-sequence (m=7, f_b=8 GHz)

Figure 3.8: Comparison of the SNR for different levels of signal attenuation.

3.3.4 Effect of the antenna array on the SNR

Figure 3.9 shows the SNR for both stimulus signal types when a real antenna system is simulated with a clock jitter of 1.5 ps RMS. The transmitted peak-to-peak voltages were chosen such that the peak-to-peak voltage at the receiver is equal to the T&H input range for both signal types. There is no significant difference in the SNRs of the two cases, indicating that high levels of jitter have a severely detrimental effect on the performance when using an M-sequence.

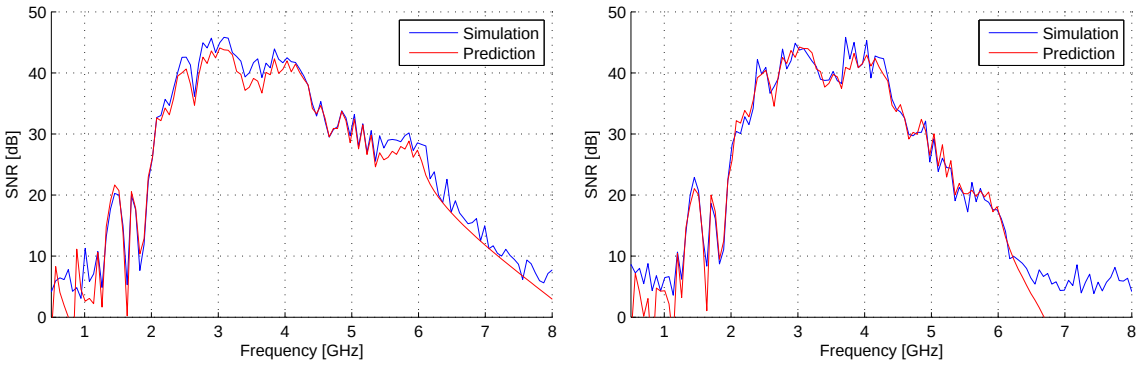

(a) Pulse train **(b)** M-sequence (m=7, f_b=8 GHz)

Figure 3.9: SNR for a systems using a simulated transfer function of distant antennas.

If there exists additional signal attenuation between the two antennas, as would be the case when a coupling fluid is used, the M-sequence results in better performance. This is shown in Figure 3.10 where an additional 20 dB of attenuation was placed between transmitter and receiver. The plots also show the predicted SNR based on (3.17), which is in good agreement with the simulated values.

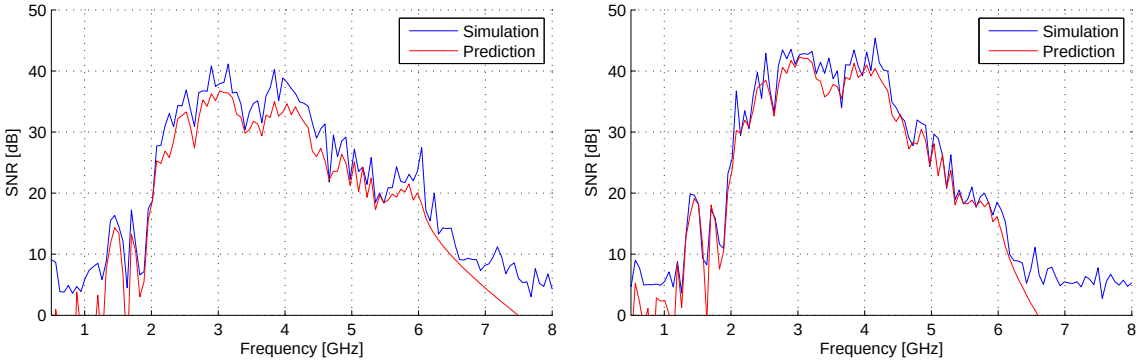

(a) Pulse train **(b)** M-sequence (m=7, f_b=8 GHz)

Figure 3.10: SNR for a systems using a simulated transfer function of distant antennas with an addition 20 dB attenuation.

4

Prototype implementation

This chapter discusses the laboratory instruments, off-the-shelf components and their settings used to implement the prototype. The theory and design aspects of the signal generator, amplifiers, data conversion, PLL and FPGA subsystems are discussed. The antenna array is discussed in [9] and will not be repeated here.

4.1 The complete system

A block diagram of the complete system is shown in Figure 4.1, with the component details listed in Table 4.1. The subsections of the system are described in more detail in the following sections.

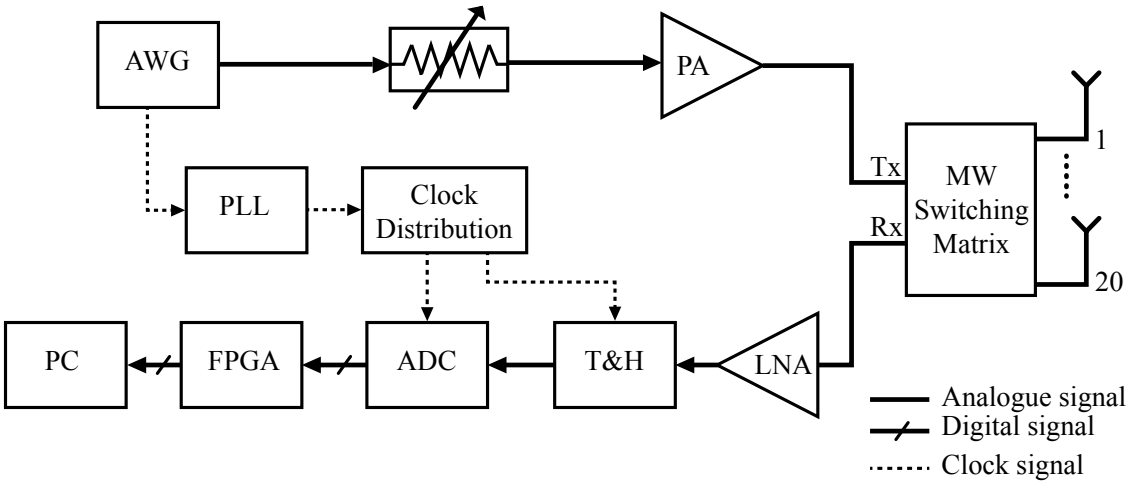

Figure 4.1: System block diagram of the complete time-domain system. AWG=arbitrary waveform generator, PA=power amplifier, PLL=phase-locked loop, LNA=low-noise amplifier, T&H=track-and-hold and ADC=analogue-to-digital converter.

Component/Instrument	Model no.	Manufacturer
AWG (laboratory instrument)	AWG7102	Tektronix
Power amplifier (connectorized module)	ZHL-42W	Mini Circuits
PLL (evaluation module)	AD9520/ADF4351	Analog Devices
Clock distribution (evaluation module)	AD9508	Analog Devices
LNA (evaluation module)	HMC639ST89E	Hittite
T&H (evaluation module)	HMC760LC4B	Hittite
ADC (evaluation module)	ADS41B29	Texas Instruments
FPGA (development board)	ML605	Xilinx
Switching matrix (laboratory instrument)	CXM/128-S	Cytec Corp.

Table 4.1: List of components and instruments used in the system.

4.2 Signal generation

Suitable off-the-shelf components capable of generating the pulse trains and M-sequences could not be found on the market. This is believed to be due to both limits of the current solid state technologies and lack of industry demand for such devices. Simple circuits for pulse train generators based on the step recovery diode are proposed in [35] and [38]. These circuits also allow for coarse control of the pulse width and thus signal bandwidth. Unfortunately such pulse generators suffer from high levels of jitter and are therefore not suitable for this application [17]. As for the M-sequence, monolithic linear feedback shift registers operating at the desired frequencies are available from Adsantec [1]. Unfortunately the only available shift register lengths are m=7 and m=15, which results in an inadequate frequency resolution or an excessively long measurement time respectively.

The signals were therefore generated by an AWG7102 arbitrary waveform generator (AWG) from Tektronix. This laboratory instrument performs a digital-to-analogue conversion on specified samples at up to 10 GHz, with a jitter level of 0.9 ps RMS and an output bandwidth of 3.5 GHz which is less than the desired 4 GHz bandwidth [32]. The AWG sample output rate is adjustable and is equal to f_b when an M-sequence is generated. Unless otherwise stated, the generated signals have an output amplitude of 0.5 V peak-to-peak. The AWG has two output channels which were used to generate the stimulus signal and the reference clock with frequency f_{rep}. Both signals were synchronized because they are triggered by the same internal reference oscillator.

As stated in Section 2.2.2, a low-pass filter should be placed after the signal generator when using an M-sequence as stimulus signal. A Microlab LA-40N low-pass filter, which has a cutoff frequency at 4 GHz, was used for this purpose. However, it was found that the filter did not improve the SNR significantly, therefore the low-pass filter was not included in the system. Aliasing due to the sidelobes of the sinc^2 spectrum shape was also not a problem because the equivalent sampling rate used was much higher than the Nyquist rate.

4.3 Amplification

As in any wireless system, a power amplifier on the transmitting side and a low-noise amplifier (LNA) on the receiving side are required to compensate for high losses between antennas. Unfortunately, suitable components were not easily available due to wireless regulations and lack of commercial demand for UWB amplifiers. Components were therefore selected based on availability and cost, as long as they operate approximately in the range of 100 MHz to 4 GHz.

The ZHL-42W+ power amplifier from Mini Circuits, which operates from 10 to 4200 MHz, was selected because it was the only available power amplifier operating in the correct frequency range. At a supply voltage of 15 V, it has a gain of approximately 37.5 dB which may be higher than desired, depending on the type of transmitted signal. A variable attenuator was therefore placed before the power amplifier to find the best level of attenuation (see Figure 4.2). For the receiving side, an HMC639ST89E LNA from Hittite was used. This device has a gain of approximately 13 dB, a noise figure of 2.3 dB and operates over the frequency range of 200 MHz to 4 GHz.

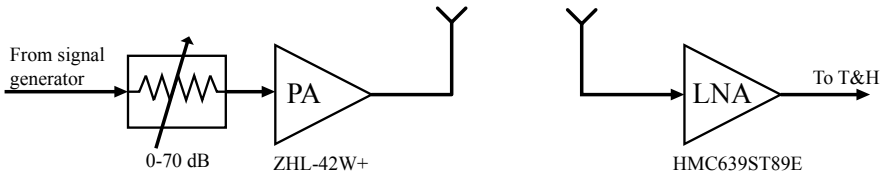

Figure 4.2: Block diagram of the amplifiers and antenna signal chain. The switching matrix has been omitted from this diagram.

4.4 Data conversion

Although equivalent-time sampling relieves the sampling rate requirements of the ADC, the input bandwidth of the sampler must still be at least as wide as the sampled signal (max 4 GHz). Current high-speed 12-bit ADCs have bandwidths up to about 2 GHz, therefore the sampling was done by an external T&H whereas the ADC only performs digitization of the approximately constant output voltage of the T&H during the hold stage (see Figure 4.3). This relieves the ADC of the high input bandwidth requirement.

The HMC760LC4B T&H from Hittite, which has an input bandwith of 5 GHz and a maximum sampling rate of 4 GHz was used for sampling. The minimum stated sampling rate of the T&H, is 250 MHz, which is higher than desired but it was found that sampling rates down to 180 MHz still yield acceptable performance. Such a high sampling rate does not result in an acceptable frequency resolution according to the relationships given in Section 2.3. Therefore an integer multiple of the sampling rate, nf_s, was used as the T&H and ADC sampling rate. The correct sampling rate was then achieved by only storing every n^{th} sample.

The ADS41B29 ADC with an input bandwidth of only 800 MHz, maximum sampling rate of 250 MHz, resolution of 12 bits and input range of 1.5 V_{pp} was

selected for digitization. According to the datasheets, a total aperture jitter of 122 fs RMS is added to the total jitter in the system by the selected T&H and ADC. As is seen in Figure 4.3, a phase shift between the T&H and ADC sampling clocks is required such that the ADC sample is taken during the hold stage and not the track stage. This problem is discussed next.

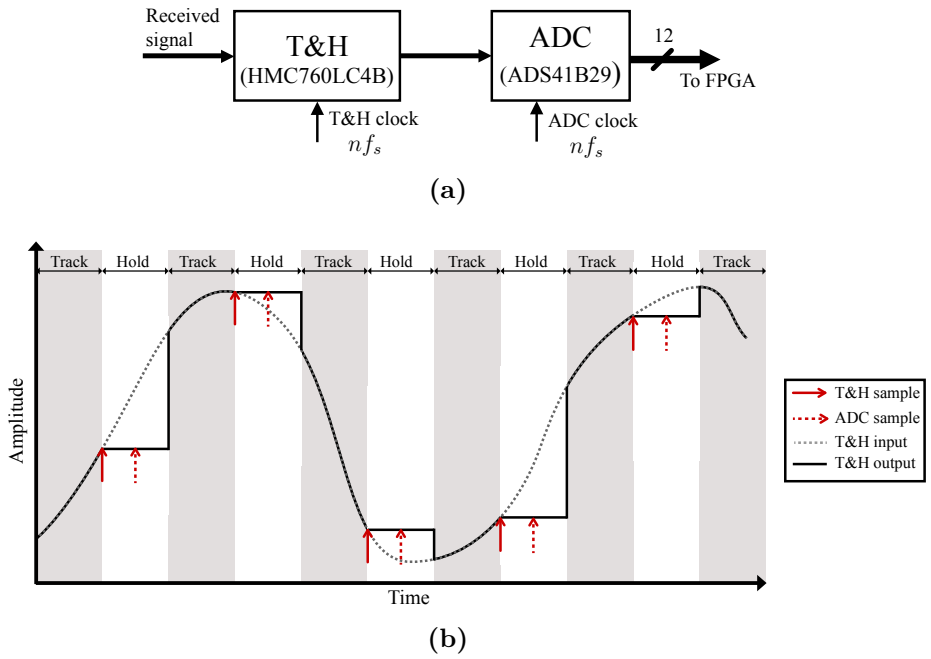

Figure 4.3: Illustrations of a) the data conversion system and b) the ideal T&H sampling sampling process.

4.5 Clock synthesis

4.5.1 Clock generation scheme

Relationships (2.9) and (2.10) show that only a single stable oscillator is needed in the system because all clock frequencies are strictly related. The clock from which all other clocks are synthesized was chosen to be the oscillator clocking the signal generator. In the case of a pulse train generator this oscillator has a center frequency of f_{rep}. For an M-sequence generator the oscillator must generate a clock with frequency f_b, which is an integer multiple of f_{rep}. A prescaler with a value of $2^m - 1$ can therefore be used to divide f_b down to f_{rep}. The purpose of the clock generator is then to synthesize a sampling clock with frequency f_s from a clock with frequency f_{rep} by satisfying the relationship

$$f_s = \frac{N_s}{N_s + 1} f_{rep} \tag{4.1}$$

which was derived by combining (2.9) and (2.10). The ADC clock can be generated using a frequency divider and multiplier as shown in Figure 4.4. These operations can be implemented using a phase-locked loop (PLL). PLLs are common components

in communication systems and integrated PLLs are therefore widely available at low costs, while offering programmable frequency scaling ratios. This approach to clock generation was therefore selected.

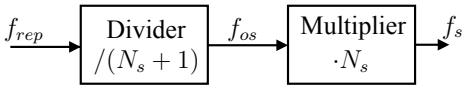

Figure 4.4: Block diagram of a clock divider and multiplier that can be used to generate the ADC clock frequency f_s.

4.5.2 Frequency synthesis using PLLs

As discussed above, a PLL was chosen to synthesize the sampling clock with a frequency f_s from a reference clock with a frequency f_{rep} coming from the signal generator. An integer-N PLL (Figure 4.5) synthesizes a clock with frequency f_{out} from a reference frequency f_{ref} according to the relationship

$$f_{out} = \frac{N}{R} f_{ref} \tag{4.2}$$

where N and R are integers. The synthesis task is then easily accomplished by setting $N = N_s$ and $R = N_s + 1$. However, this solution may result in an output with severe phase noise as will now be described.

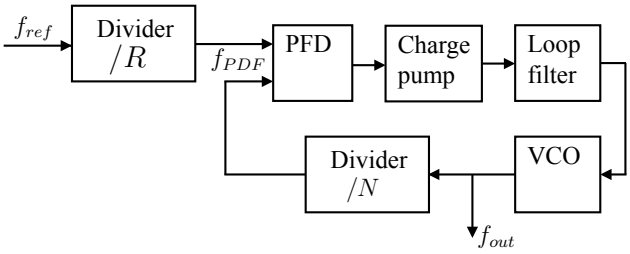

Figure 4.5: Block diagram of a PLL frequency synthesizer. PFD=phase frequency detector, VCO=voltage controlled oscillator.

4.5.3 Phase noise from internal sources

The output phase noise of a PLL is contributed to by both the PLL internals and phase noise from the reference input signal. The phase noise of the reference signal is dependent on the signal generator and will be neglected here. The output in-band phase noise of the PLL, normalized to 1 Hz, is then approximately [3]

$$L_{1\text{Hz}}\ [\text{dBc/Hz}] = L_{PLL} - 20\log(N) - 10\log(f_{PFD}) \tag{4.3}$$

where L_{PLL} is the phase noise generated by the PLL[1] and f_{PFD} is the input frequency of the phase-frequency detector (PFD) in the PLL and is equal to f_{ref}/R. In this

[1]This parameter is known as the PLL figure of merit and is stated in the datasheet.

system, N_s can be from a few hundred to 9999 samples, therefore if $R = N_s + 1$, f_{PFD} will be very low, resulting in severe phase noise. A higher f_{PFD} will allow a proportional decrease in N while preserving the frequency scaling according to (4.2). However, according to (4.3) the phase noise has a $-20\log_{10}$ dependence on N and only a $-10\log_{10}$ dependency on f_{rep} resulting in reduced phase noise.

This can only be done if N may take on fractional values, which is possible with a fractional-N PLL. The drawback of fractional-N PLLs is that the fractional division is implemented using a sigma-delta converter, which produces spurs. Spurs do not contribute significantly to jitter [21], but they can be removed by adding a small amount of white noise within the PLL. The addition of white noise almost eliminates the spurs but increases the entire noise floor. In order to find the best configuration, both integer-N and fractional-N PLL (low-noise and low-spur modes) implementations of the clock generator were tested.

4.5.4 Phase noise from the reference signal

Phase noise from the reference input $L_{ref}(f_m)$, where f_m is the frequency offset from the center frequency, passes to the output according to the relationship [4]

$$L_{out}(f_m) = |H_{PLL}(f_m)|^2 \frac{N^2}{R^2} L_{ref}(f_m) \tag{4.4}$$

where $H_{PLL}(f_m)$ is the loop transfer function, which is proportional to the loop filter transfer function and charge pump current and has a low-pass response [4]. While the details of this relationship are not important, it should be mentioned that the amount of reference phase noise passed to the output of the PLL is controlled by $H_{PLL}(f_m)$. Control of the charge pump current of the PLL offers some control over the cutoff frequency of $H_{PLL}(f_m)$. An increase in charge pump current widens the loop bandwidth, passing more reference phase noise, but allows for a more stable operation at a high f_{PFD}. The system was therefore tested at different charge pump currents to investigate how this trade-off affects the measurement accuracy.

4.5.5 Clock generation system

In the previous generation of this system, the T&H clock and phase shifted ADC clock were synthesised using a direct digital synthesizer (DDS), however this device is not capable of implementing the desired frequency scaling and therefore required a laboratory synthesizer. A PLL is able to synthesize the sampling clock from the reference clock generated by the signal generator (AWG) without any additional synthesizer. The phase shift between the T&H and ADC sampling clocks was implemented by firstly generating an even higher multiple of the sampling frequency with the PLL: $f_{PLL,out} = DIV \cdot nf_s$, where DIV is an integer. By counting C cycles of this high frequency clock, a phase shift of

$$\Delta\theta \text{ [deg]} = \frac{360^\circ}{DIV} \cdot C \tag{4.5}$$

can be implemented. By dividing the PLL output frequency by DIV, the T&H and ADC sampling rate of nf_s is generated. The result is two clocks with a frequency

of nf_s and a phase shift of $\Delta\theta$ relative to one another. This strategy is depicted in Figure 4.6.

Both the AD9520 integer-N PLL and ADF4351 fractional-N PLL from Analog Devices were tested and their performance compared. The ADF4351 allows for both a low-noise mode and low-spur mode. For the division by DIV and phase shift of $\Delta\theta$, the AD9508 clock distributor was used. Software was written to determine suitable AWG, PLL and clock generation parameters based on the desired f_{rep}, N_s, m and f_b.

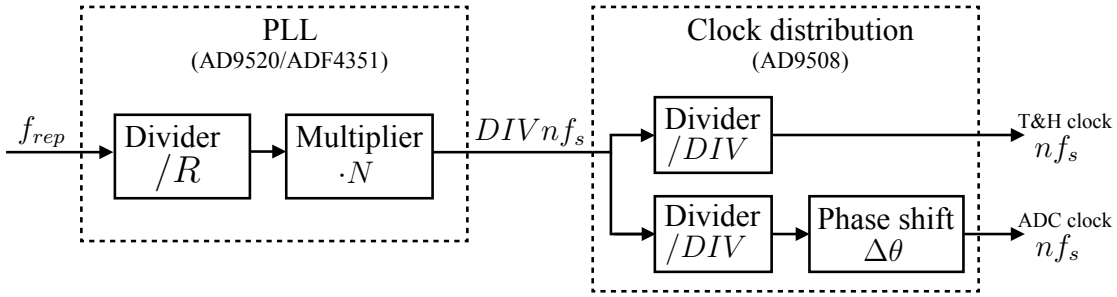

Figure 4.6: Block diagram of the clock generation system implementation.

4.6 Digital system

The ML605 FPGA development board was used to maintain synchronization, perform averaging and to transfer the measured samples to a PC. As is shown in Figure 4.7, the ADC samples enter the FPGA at a sampling rate of nf_s. The digital hardware was then designed to only store every n^{th} sample in local block memory. A digital counter within the Synchronization Unit cycles through N_s samples, producing the FPGA sampling trigger with frequency f_{os}, as depicted in Figure 2.3. This clock keeps track of the start of the period such that multiple periods can be recorded with the same phase. This is required for both calibration and averaging purposes.

The FPGA also hosts an embedded processing core, which runs firmware for reconfiguring the harware parameters (n, N_s and N_{ave}), performing coherent averaging and communicating with a PC via USB. The parameters' maxima that the system is capable of are N_s=9999, n=256 and N_{ave}=128. Software was written for letting the user specify the measurement parameters, load them to the FPGA hardware and run a measurement sequence (see Figure 4.8). This software also runs the operation of the switching matrix. At the end of a measurement sequence, the data is transmitted to the PC at 203400 bits/s for image reconstruction.

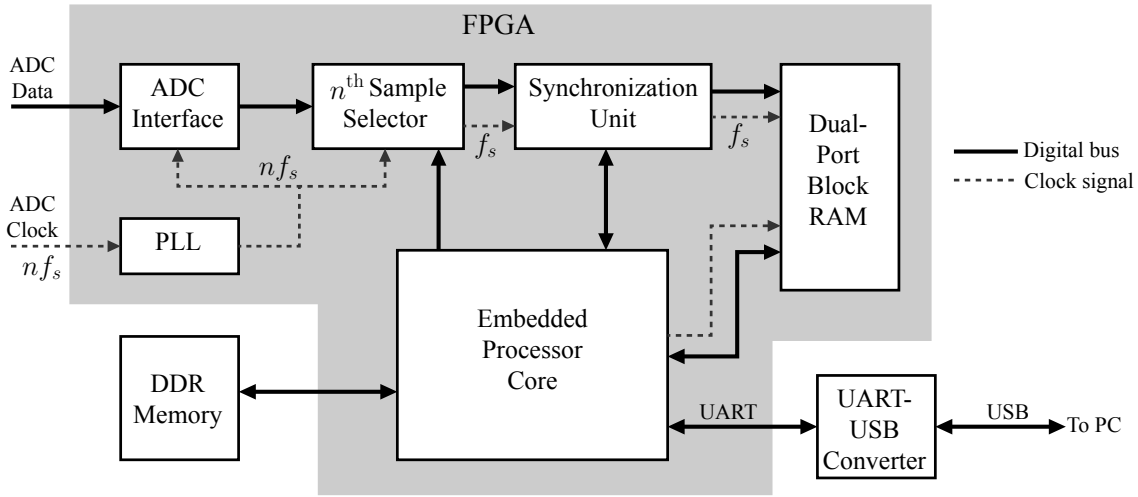

Figure 4.7: Block diagram of the digital hardware implemented on the ML605 FPGA development board.

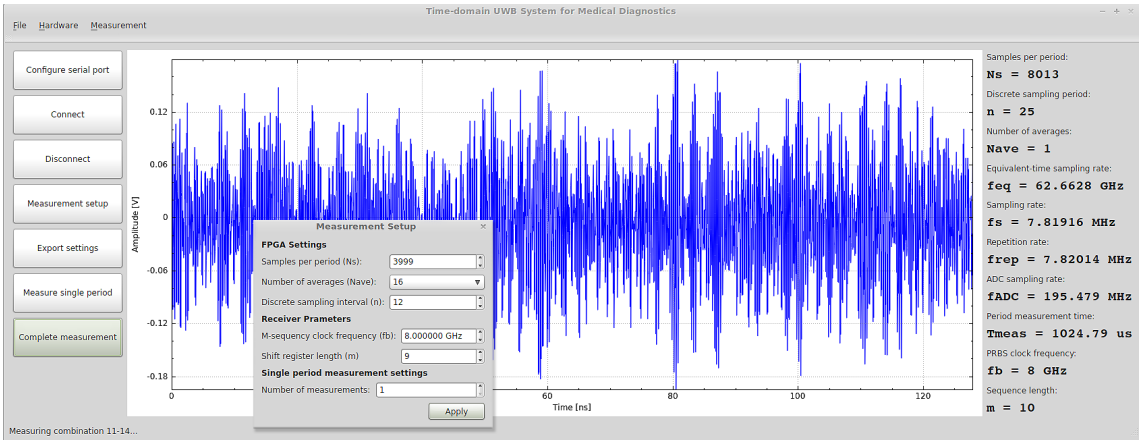

Figure 4.8: Screenshot of the software used to control the measurement system.

5

Performance evaluation

In this chapter the optimal system settings are investigated and the performance of the system is evaluated and compared to that of an E8362B VNA from Agilent Technologies. Finally, image reconstructions were performed on the measured data. Unless otherwise stated, the AWG output was directly connected to the T&H input for testing the performance of the transmitter and receiver only.

5.1 Determination of optimal settings

The purpose of the results shown in this section was to find the system parameters, clock generation method and stimulus signal yielding the best system performance.

5.1.1 Effect of f_{eq} and m on the SNR

To find the most suitable equivalent sampling rate f_{eq} and shift register length m for an M-sequence, the SNR was compared for different values of these parameters. Figure 5.1a shows the effect of the equivalent sampling rate f_{eq} on the total SNR, computed using (3.15). Parameters were chosen such that there is a constant f_{rep} of 31.88 MHz in all cases. From f_{eq} = 15.6 to 62.65 GHz the SNR is proportional to N_s, as predicted by (3.17). The low-pass filter to suppress the sidelobes of the M-sequence spectrum was not included in the system, therefore aliasing reduces the SNR at a lower f_{eq}. At f_{eq} = 125.4 GHz the phase noise spectra has been widened by such a high factor $N_p = N_s + 1$ that significant overlap with neighbouring harmonics reduces the SNR, as was illustrated by Figure 3.4. An f_{eq} of 62.65 GHz is the best of the measured cases as it results in the highest SNR and fast measurements.

According to the equation for average power of an M-sequence (2.7) and the jitter model derived in Section 3.2.2, the shift register length m should not have an impact on the SNR. However Figure 5.1b shows the opposite. The parameters were chosen such that all cases have an equivalent sampling rate of approximately f_{eq}= 31.4 GHz. The low SNR for m=10 can again be explained by the phase noise spectrum overlap between closely neighbouring harmonics. The reason for the lower SNR for m=7 is not known. The best shift register length for this level of jitter according to the plot is m=9. This gives a total of 255 frequency points within the bandwidth and a frequency resolution of 15.656 MHz when the bandwidth is 4 GHz.

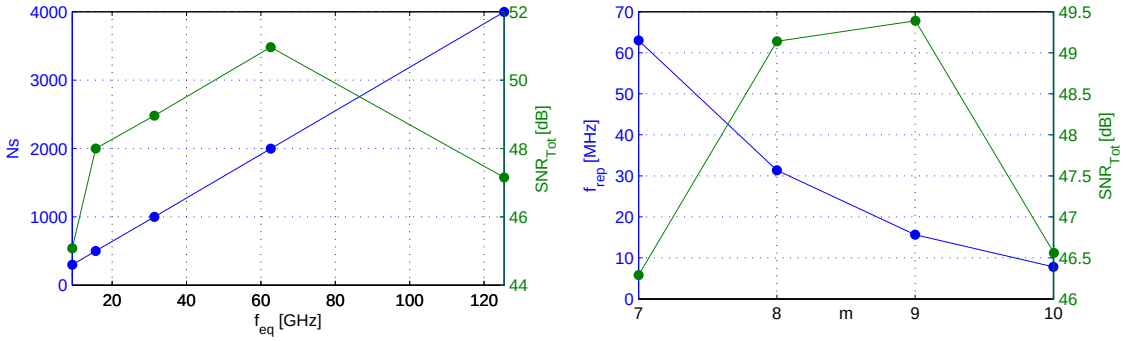

(a) **(b)**

Figure 5.1: Plots of the SNR as a function of a) equivalent-time sampling rate f_{eq} and b) shift register length m and , $f_b = 8$ GHz. The corresponding N_s and f_{rep} is also plotted in the respective cases.

5.1.2 Comparison of clock generation methods

Figure 5.2 shows the SNR for both stimulus signals when different sampling clock generation methods are used. Parameters have been chosen such that the frequency resolution f_{rep} is equal to 10 MHz for both signals, allowing a curve-to-curve comparison. The clock generation method has little effect on the SNR of a pulse train system, indicating that the SNR is limited by the low signal power instead of timing jitter. For the M-sequence, the clock generation method has a significant effect and as expected from theory, the fractional-N PLL gives the best performance due to it's low jitter. The low-noise mode gives the best performance, confirming that spurious signals do not have a significant effect on timing jitter. The decrease in SNR with frequency for an M-sequence occurs because of the increased effect of jitter at higher frequencies, as predicted by the model derived in Section 3.2.2 and a drop in signal power due to the sinc^2 shaped power spectrum.

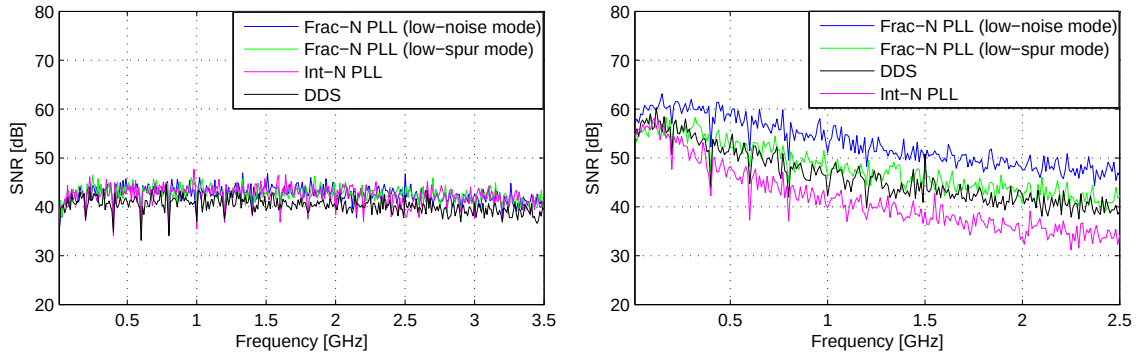

(a) Pulse train **(b)** M-sequence (m=9, $f_b = 5.11$ GHz)

Figure 5.2: Comparison of the SNR for different clock generation methods.

Clock generation using a DDS, which requires an additional laboratory synthesizer, was also tested for comparison with the clock generation technique of the previous system. The SNR for the DDS system is 8 dB lower than when using the fractional-N PLL. The integer-N PLL results in even worse performance because of its low PFD frequency. The new clock generator therefore yields a higher SNR and is more compact than the previous DDS-based clock generator

5.1.3 Effect of charge pump current on the SNR

As mentioned above, the charge pump current I_{CP} of the fractional-N PLL gives some control of the PLL loop bandwidth and therefore affects the PLL performance. In order to find the best setting, a 4 GHz sinusoid was sampled using a clock generated with the fractional-N PLL under different charge pump settings. Figure 5.3 shows the resulting SNR and relative jitter for both noise modes as a function of charge pump current. A negative correlation between SNR and relative jitter can be observed. The low-noise mode clearly provides better performance, with the best chosen case to be I_{CP}= 2.81 mA because of both high SNR and low jitter. The decrease in SNR (or increase in jitter) with increasing I_{CP} for the low-spur case can be attributed to a widening loop bandwidth, passing more of the white noise added to remove the spurs.

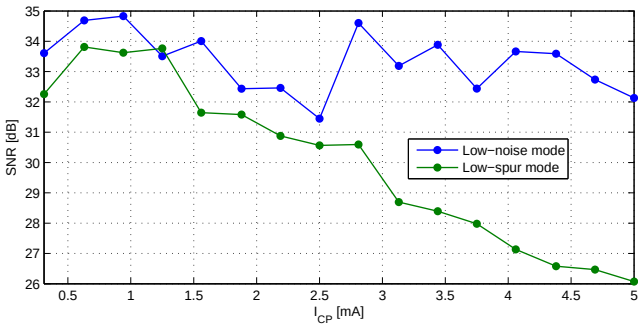

(a)

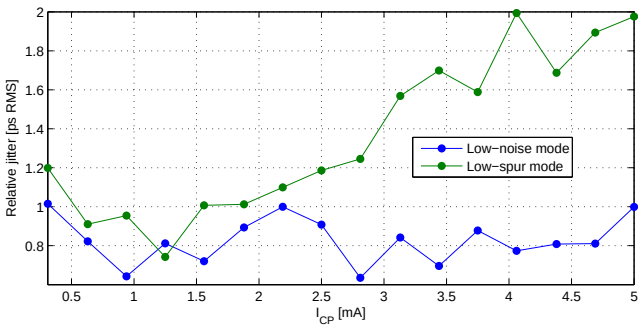

(b)

Figure 5.3: Plots of a) the SNR and b) jitter for both the low-noise and low-spur modes of the fractional-N PLL for different charge pump currents.

The relative jitter shown in Figure 5.3b is the jitter of the clock relative to the cycle-to-cycle jitter of the generated signal. In this application, the relative jitter mostly contains jitter information from the clock generation system, which is of most interest. The relative jitter was estimated by sampling a 4 GHz sinusoid using the prototype and reconstructing the signal using a Fourier series with much higher temporal resolution. A temporal resolution of approximately 40 fs was used to give an accurate measure of the relative jitter. The zero-crossing locations of this high resolution signal were then subtracted from the theoretical zero-crossing locations to obtain the relative jitter.

5.1.4 Optimal system configuration

Based on the previous investigations, the best performance can be expected with the parameters summarised in Tables 5.1 and 5.2. Figure 5.4 shows SNR for the settings yielding the best performance, along with the SNR of the previous generation of the UWB time domain system. The new system has a SNR above 44 dB up to the desired bandwidth of 4 GHz and the improvement in SNR compared to the previous system is clear. This SNR was tested for a 0.5 V peak-to-peak input to the T&H, which is its full-scale range, therefore the SNR curve in Figure 5.4 is equivalent to the dynamic range of the system. The dynamic range of the VNA is approximately 120 dB, which is significantly higher than that of the current time domain system.

Parameter	**Value**
Stimulus signal type	M-sequence
Signal generator clock f_b	8 GHz
Shift register length m	9
Samples per period N_s	3999
Repetition rate f_{rep}	15.6556 MHz
Sampling rate f_s	15.6517 MHz
Equivalent sampling rate f_{eq}	62.6067 GHz
T&H/ADC sampling rate nf_s	187.82 MHz

Table 5.1: List of the final stimulus signal and sampling parameters.

Parameter	**Value**
Clock generator type	Fractional-N PLL
PLL reference divider R	3
PLL multiplier N	287.928
PLL noise mode	Low-noise
PLL charge pump current I_{CP}	2.81 mA
Clock distribution divider DIV	8
Clock distribution phase shift $\Delta\theta$	270°

Table 5.2: List of the final clock generator parameters.

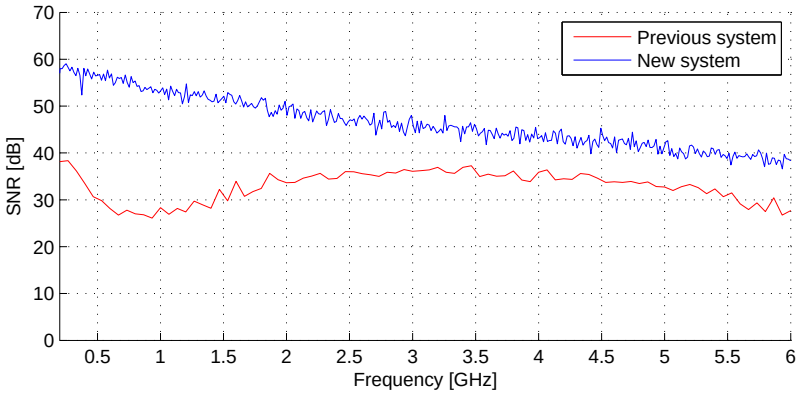

Figure 5.4: Plots of the SNR for the current and the previous time-domain systems, both under single-ended drive.

5.2 Noise performance evaluation

5.2.1 Effect of signal averaging on the SNR

Figure 5.5 shows the improvement in SNR due to signal averaging for both a pulse and PN sequence. As predicted by (3.17), SNR [dB] is proportional to $10\log(N_{ave})$. Signal averaging can therefore be performed to increase the SNR at the cost of increased measurement time and the effect is equal for both the pulse and M-sequence.

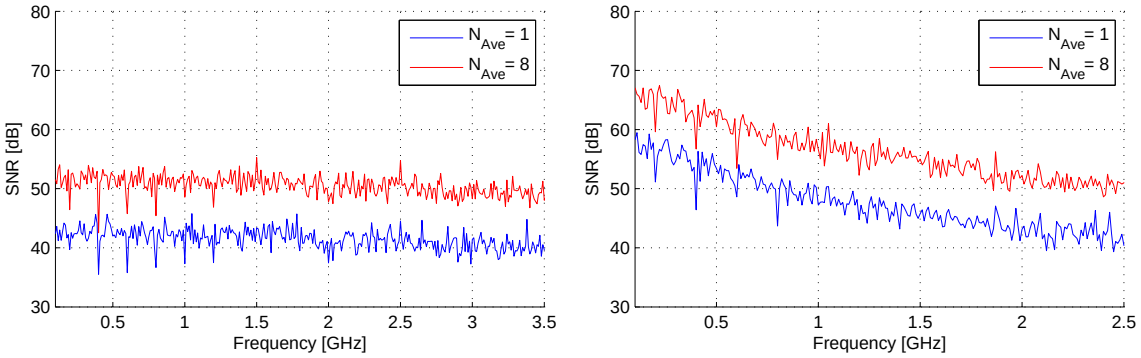

(a) Pulse train **(b)** M-sequence (m=9, f_b = 5.11 GHz)

Figure 5.5: Comparison of the SNR for with and without signal averaging.

5.2.2 Effect of signal attenuation on SNR

To investigate the effect of signal attenuation on SNR for both a pulse train and M-sequence, a variable attenuator was inserted between the signal generator and T&H and the attenuation was varied. The peak-to-peak voltages were set to 500 mV for both signals. The results are shown in Figure 5.6. Parameters were chosen such that f_{rep} and N_s are equal for both signals, allowing a comparison of the SNR. The SNR [dB] of a pulse train decreases proportionally to the amount of attenuation, but for the M-sequence the SNR [dB] does not vary significantly for low levels of

attenuation. This indicates that the SNR of the M-sequence is limited by jitter. At higher levels of attenuation, the noise due to jitter is decreased, giving a linear relationship between SNR [dB] and attenuation level for an M-sequence.

The plots also shows that if the effect of jitter is negligible (at an attenuation of 30 dB and more in this case) an SNR improvement of approximately 25 dB can be expected when using an M-sequence instead of a pulse train at the same peak-to-peak voltages. Therefore even at moderate levels of jitter, an M-sequence with a low peak-to-peak voltage results in an improved SNR and less demanding power amplifier requirements compared to when using a pulse train as the stimulus signal.

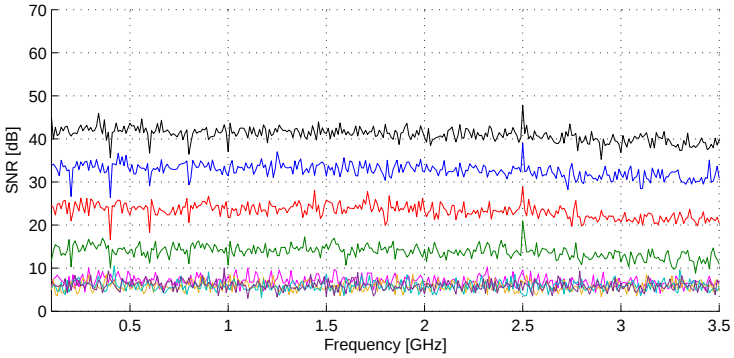

(a) Pulse train

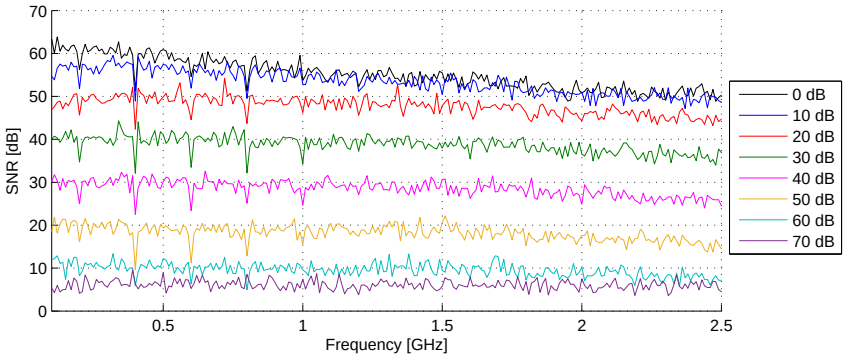

(b) M-sequence (m=9, $f_b = 8$ GHz)

Figure 5.6: Comparison of the SNR for varying levels of signal attenuation.

5.2.3 Measurement of transmission coefficients

In order to test the system's capability of characterizing a linear system, the insertion loss of different attenuator values were measured both using this time domain system and a VNA. The VNA start and stop frequencies were set to 15.55577 MHz to 4.6966773 GHz respectively with 300 points, giving approximately the same frequency points as measured with the time domain system.

Figure 5.7 shows the resulting magnitude measurements of S_{21} with signal averaging applied ($N_{ave} = 32$). $|S_{21}|$ can be approximated with up to 60 dB of attenuation over the entire frequency range, which (taking averaging into account) agrees with the dynamic range of 44 dB at 4 GHz. Figure 5.8 shows the root mean squared error (RMSE) between the VNA and time-domain system measurements

for both the magnitude in decibels and the phase of S_{21}, with and without signal averaging applied. An increase in RMSE can be observed for both the measured magnitude and phase as attenuation increases, but signal averaging provides a significant improvement.

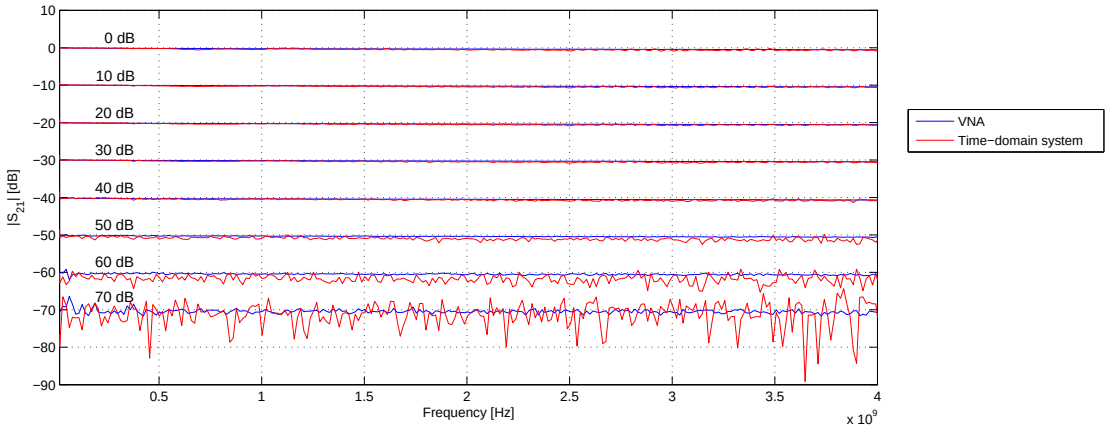

Figure 5.7: Comparison of measured transmission coefficient magnitudes for different attenuator values as measured by a VNA and the time-domain system. The attenuator value is shown above the respective curve. Signal averaging was applied with $N_{ave} = 32$.

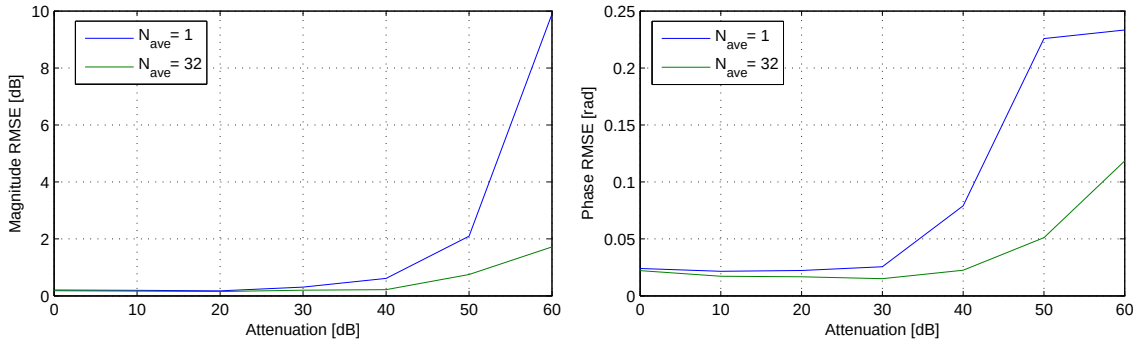

(a) Magnitude RMSE **(b)** Phase RMSE

Figure 5.8: Root mean squared error between the VNA and time-domain measurements of S_{21} with and without averaging.

5.2.4 Effects of the antenna array on the SNR

The overall system SNR includes the effects of the switching matrix and antenna array. The results are shown in Figure 5.9. The SNR of the M-sequence system is higher than that of the pulse train system in all cases except for within the frequencey range of 2.5 to 4 GHz when the transmitting and receiving antennas are neighbouring. This is because at this high power level, a large amount of M-sequence power is converted to noise due to jitter. This is verified by observing the noise spectra in Figure 5.9 of the two cases shown.

The sampling settings chosen are listed in Table 5.3. The sampling parameters are different for the two signals and correspond to the parameters of the previous system for the pulse train and the optimal system configuration for the M-sequence. These parameters show that even for a measurement performed four times faster (lower N_s), with 6 dB more attenuation and with a frequency resolution only 5.7 MHz greater than that of a pulse train system, the M-sequence system yields better performance in most cases. However, the timing jitter must be reduced in order to gain the full performance improvement that can be obtained when using an M-sequence as stimulus signal. It is suspected that the AWG is the primary contributor of timing jitter in the system.

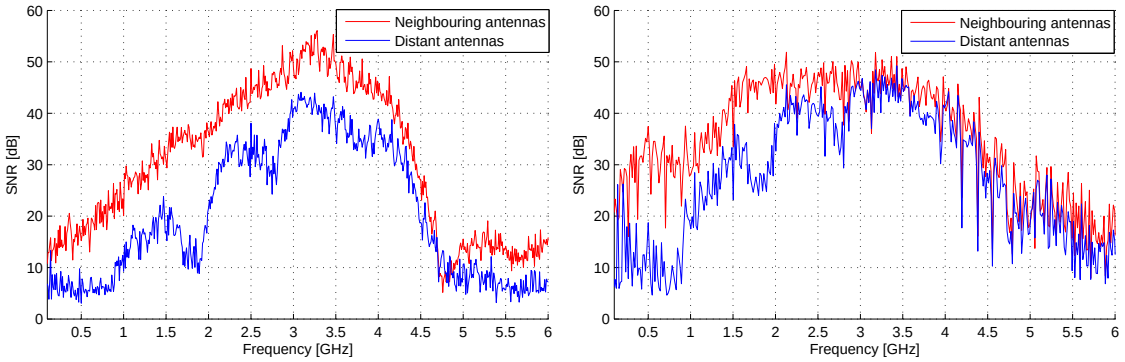

(a) Pulse train **(b)** M-sequence (m=9, $f_b = 8$ GHz)

Figure 5.9: Comparison of the SNR of the complete system when the transmitter and receiver are connected to neighbouring antennas and distant antennas.

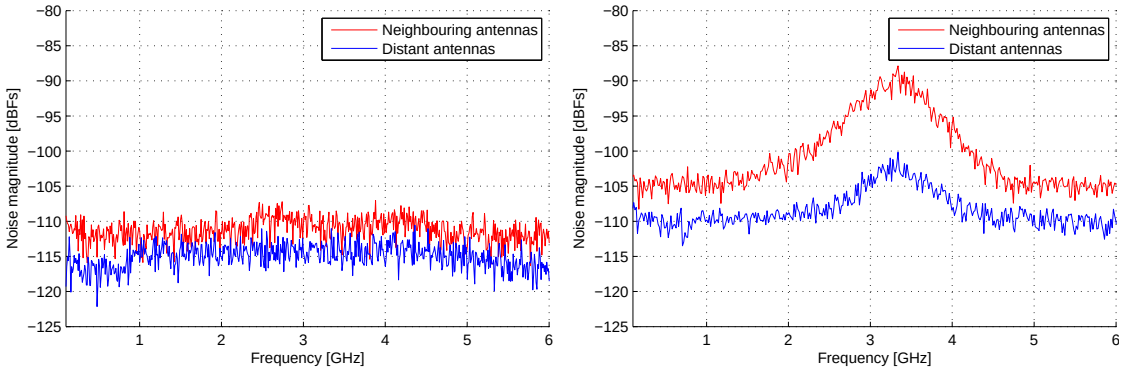

(a) Pulse train **(b)** M-sequence (m=9, $f_b = 8$ GHz)

Figure 5.10: Comparison of the noise spectra for the measurements used to obtain Figure 5.9.

Parameter	Value (Pulse train)	Value (M-sequence)
Samples per period N_s	9999	3999
Repetition rate f_{rep} [MHz]	10.000	15.656
Equivalent sampling rate f_{eq} [GHz]	99.990	62.607
Period measurement time $1/f_{os}$ [ms]	1.000	0.2555
Variable attenuator value [dB]	0	6

Table 5.3: Sampling parameters for the results shown in Figures 5.9 and 5.10.

5.3 Imaging

5.3.1 Measurement speed

The duration of a complete measurement sequence is the sum of the time taken to sample the signal, perform signal averages, switch between antennas and transmit the data to a PC. The measurement time is therefore dependent on N_s, N_{ave} and f_{rep}. Table 5.4 list some examples of measurement times. The antenna switching and data transmission contributed the most towards the total measurement time.

Stimulus signal	N_s	N_{ave}	f_{rep} [MHz]	Total measurement time [s]
Pulse train	9999	1	10	250
Pulse train	9999	16	10	304
M-sequence (m=9)	3999	1	15.656	152
M-sequence (m=9)	3999	16	15.656	169
M-sequence (m=9)	3999	128	15.656	325

Table 5.4: Measurement times for a complete measurement under different system settings.

5.3.2 Imaging reconstruction quality

The reconstructed relative permittivity and conductivity for a cylindrical beaker with a diameter of 6.8 cm filled with rapeseed oil are shown in Figure 5.11. A photo of the setup is shown in Figure 5.12. The spatial size of each pixel is 2×2 mm. The interrogating field used in the reconstruction algorithm had a center frequency of 3 GHz and a bandwidth of 300 MHz and the images shown are the results of the 20^{th} iteration.

The reconstruction of conductivity was unsuccessful in all cases because the low conductivity of oil results in the real part of the complex permittivity to be much larger than the imaginary part, whereas the reconstruction works best when the real and imaginary parts are of the same order [10]. While relative permittivity reconstruction was successful, there is no significant evidence that the choice of stimulus signal or number of coherent averages affect the reconstruction quality. This indicates that the reconstruction quality is limited by the reconstruction algorithm instead of measurement accuracy.

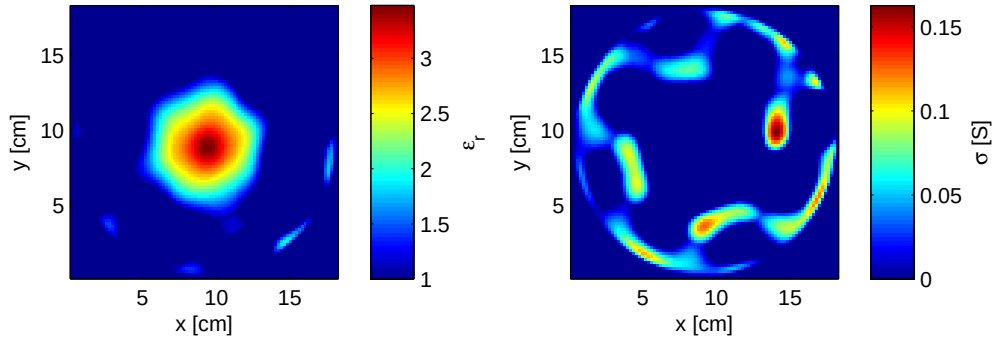

(a) Pulse train, no averaging

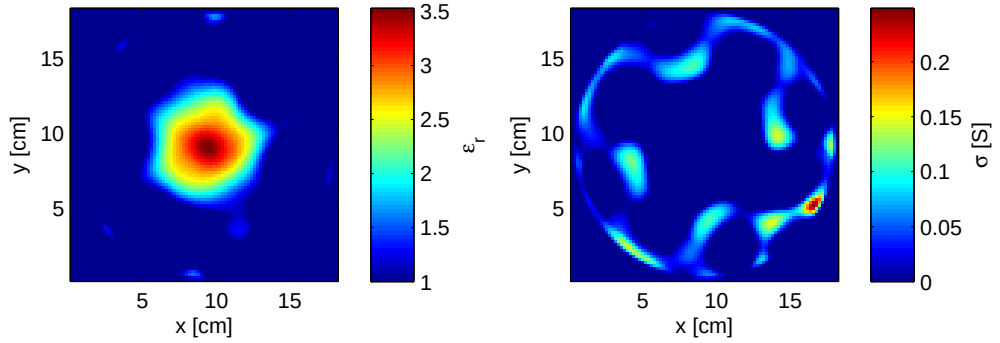

(b) M-sequence (m=9, $f_b = 8$ GHz), no averaging

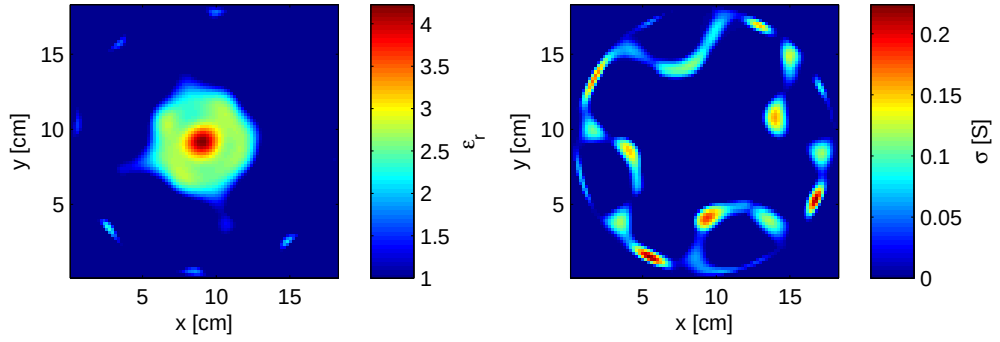

(c) M-sequence (m=9, $f_b = 8$ GHz), 16 averages

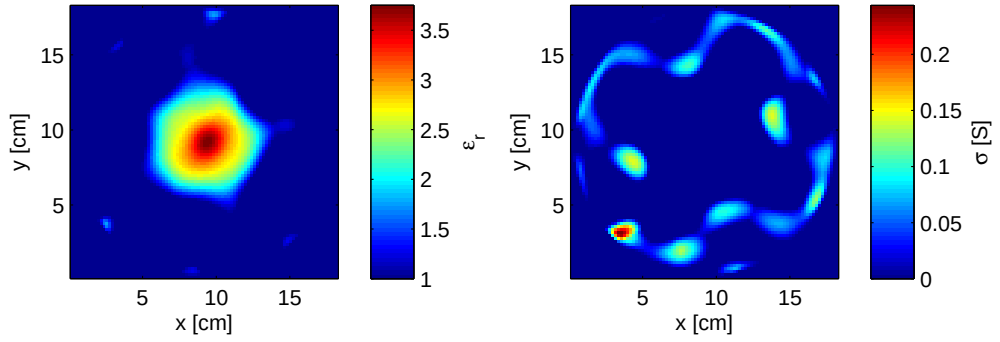

(d) M-sequence (m=9, $f_b = 8$ GHz), 128 averages

Figure 5.11: Reconstructed images of an oil cylinder with a diameter of 6.8 cm.

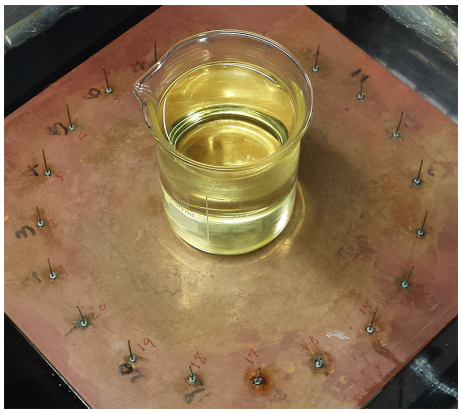

Figure 5.12: Photo of the oil cylinder with a diameter of 6.8 cm.

In order to test the system's capability of imaging an object with a size similar to a human breast, an oil-filled cylinder with a diameter of 10.5 cm was imaged. The reconstructed images are shown in Figure 5.14 with a photo of the setup shown in Figure 5.13. Only Figures 5.14a and 5.14c show a relative permittivity that resembles the shape of the object, but the reconstruction quality is significantly worse compared to the smaller cylinder shown in Figure 5.12. Figures 5.14b and 5.14d show a conductivity reconstruction that resembles a large cylinder, but the diameter is approximately 4 cm larger than the actual cylinder that was imaged. Images of this large cylinder could therefore not be reconstructed with acceptable quality with the hardware, reconstruction algorithm and settings used. It is possible that the spectral content of the interrogating field (2.85 to 3.15 GHz) used in the reconstruction algorithm was too high for resolving the large shape of the cylinder. Decreasing the center frequency or widening the bandwidth could result in a successful reconstruction.

As with the previous imaging test, there is no significant evidence that the choice of stimulus signal or number of averages affect the reconstruction quality.

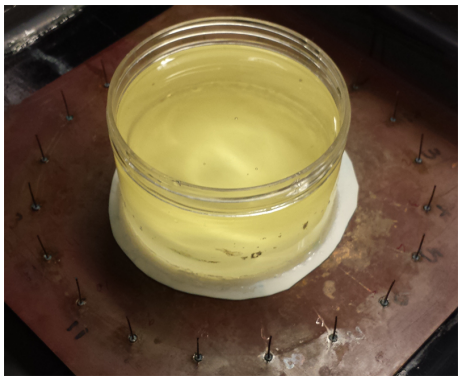

Figure 5.13: Photo of the oil cylinder with a diameter of 10.5 cm.

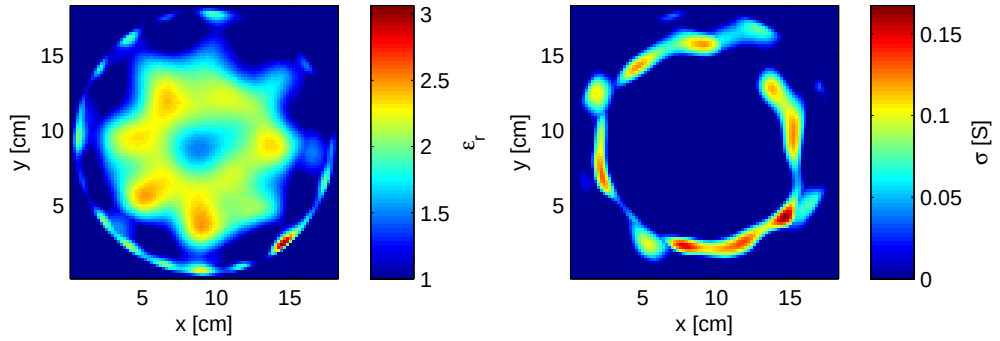

(a) Pulse train, no averaging

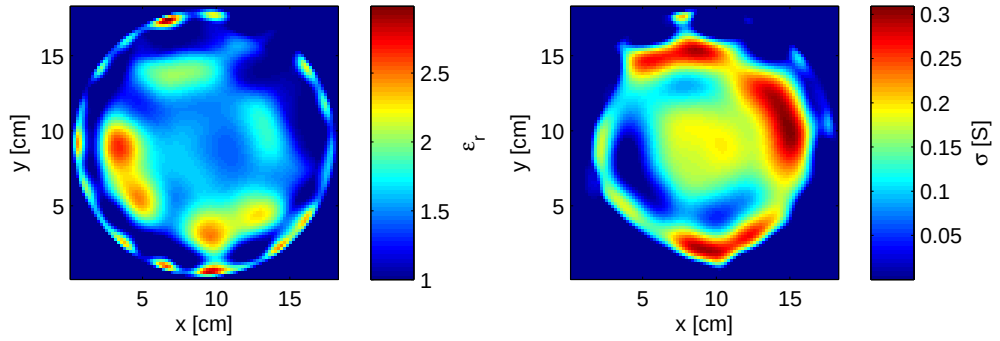

(b) Pulse train, 16 averages

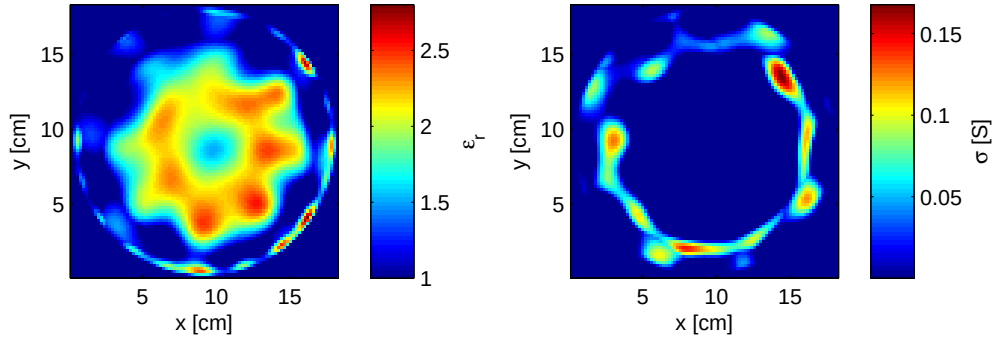

(c) M-sequence (m=9, $f_b = 8$ GHz), no averaging

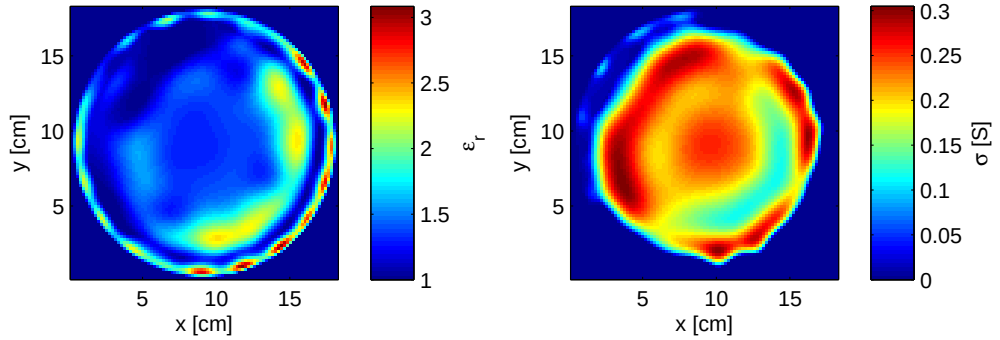

(d) M-sequence (m=9, $f_b = 8$ GHz), 16 averages

Figure 5.14: Reconstructed images of an oil cylinder with a diameter of 10.5 cm.

The electrical properties of rapeseed oil are not significantly different to those of air, resulting in weak scattering within the antenna array. In order to test the system's capability of imaging strongly scattering objects, a cylindrical phantom with a diameter of 5 cm was imaged. The phantom material, consisting of water, agar, sugar and salt, had electrical properties similar to that of human muscle tissue. A photo of the phantom is shown in Figure 5.15 with the reconstructed images shown in Figure 5.16.

Both the relative permittivity and conductivity reconstructions were successful in all cases, which is believed to be due to the higher conductivity of muscle tissue, resulting in a much higher imaginary component of the complex permittivity. However, the inner part of the phantom is not visible in the reconstructed images. This is believed to be due to significant reflections at the air-phantom boundary and a shallow penetration depth. This problem could be solved by immersing the phantom surroundings in a fluid with a characteristic impedance similar to that of muscle tissue, resulting in less significant reflections at the phantom boundary.

However, the reconstructed images still do not show significant evidence that the choice of stimulus signal or number of averages affect the reconstruction quality, indicating that the image quality is limited by the antenna setup and/or the reconstruction algorithm.

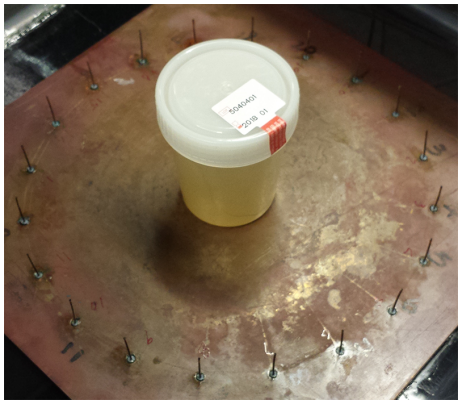

Figure 5.15: Photo of the cylindrical phantom with a diameter of 5 cm.

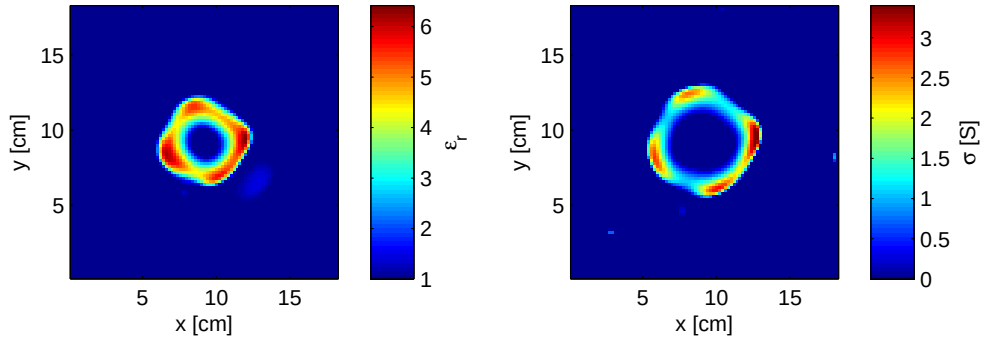

(a) Pulse train, no averaging

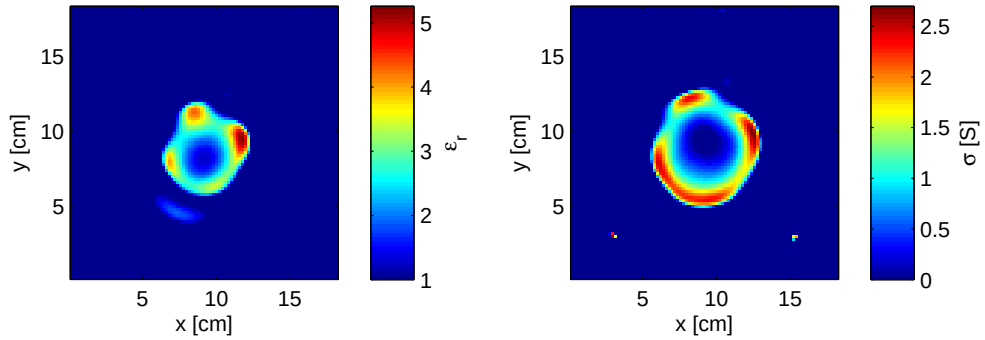

(b) M-sequence (m=9, $f_b = 8$ GHz), no averaging

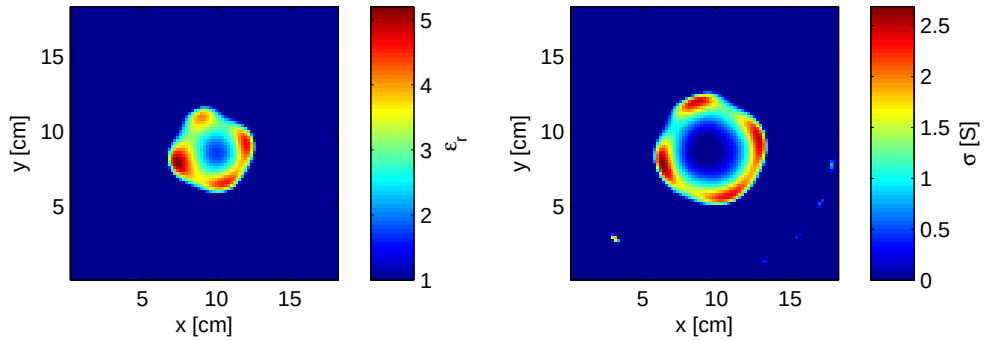

(c) M-sequence (m=9, $f_b = 8$ GHz), 16 averages

Figure 5.16: Reconstructed images of a cylindrical phantom with a diameter of 5 cm.

6
Conclusion

6.1 Summary

In this work the use of a different stimulus signal was investigated, the theory behind the equivalent-time sampling scheme was analysed and the sources of measurement errors were studied in depth. The results showed that the use of an M-sequence as a stimulus signal results in a significantly higher SNR compared to a pulse train, as long as the timing jitter is minimized. A new clocking system was therefore designed and implemented which resulted in better measurement accuracy and a more compact system compared to the previous version of the system. New digital hardware was implemented and software was written which allowed for easy reconfiguration and automated operation of the system. Imaging tests were successfully performed but it was found that the reconstruction quality was not affected by improvements investigated in this thesis. For the objects imaged, prototype and reconstruction settings used in this thesis, the measurement accuracy was not the limiting factor for the image reconstruction quality. This work has brought this technology closer to replacing a VNA and being used in clinical environments.

The major limitations of the system are firstly that a laboratory instrument needs to be used as a signal generator, the measurement speeds are longer than desired and the jitter limits the full benefit that can be obtained using an M-sequence as the stimulus signal. These limitations can be overcome as is described below.

6.2 Suggestions for future work

The following work can be done to improve the current system:

- A custom M-sequence generator will have to be designed to replace the AWG since there was no suitable off-the-shelf component available on the market at the time of writing. This signal generator can then be designed for the desired output bandwidth of 4 GHz and lower jitter than the AWG.
- A variable gain amplification system can be implemented to maximize the dynamic range for all antenna combinations. A balun can also be inserted ahead of the T&H such that twice the single-ended input peak-to-peak range can be utilized, making use of the T&H's differential input.
- A solid state switching matrix should be used instead of a mechanical switching matrix in order to significantly improve the measurement speed. Measurement speed can also be improved by implementing a high speed data transfer link between the FPGA and the PC.

- Imaging tests can be performed with different system parameters (eg. N_s, f_{eq}, f_{rep} and m) to see how the reconstructed image is affected by these parameters. A matching fluid can also be added to reduce reflections at the boundary of strongly scattering objects.

Bibliography

[1] Adsantec. *ASNT8142-KMC datasheet: Generator of DC-to-23Gbps PRBS with Selectable Polynomials*. Advanced Science And Novel Technology Company, Inc., 2014.

[2] James R Andrews. *Picosecond Pulse Generation Techniques and Pulser Capabilities*. Application Note AN-19. Picosecond Pulse Labs, November 2008.

[3] Dean Banerjee. *PLL performance, simulation and design*. Dog Ear Publishing, 2006.

[4] Roland. E Best. *Phase-Locked Loops: Design, Simulation, and Applications*. McGraw Hill, 6th edition, 2007.

[5] Richard J Collier and A Douglas Skinner. *Microwave measurements*, volume 12. IET, 2007.

[6] Shlomo Engelberg. *Random signals and noise: a mathematical introduction*. CRC Press, 2006.

[7] Shlomo Engelberg and Haim Benjamin. Pseudorandom sequences and the measurement of the frequency response. *Instrumentation & Measurement Magazine, IEEE*, 8(1):54–59, 2005.

[8] T.S. England. Dielectric properties of the human body for wave-lengths in the 1-10 cm. range. *Nature*, 166(4220):480–481, 1950.

[9] A. Fhager. Microwave tomography. *Doctoral thesis at Chalmers University of Technology*, 2006.

[10] Andreas Fhager, Parham Hashemzadeh, and Mikael Persson. Reconstruction quality and spectral content of an electromagnetic time-domain inversion algorithm. *Biomedical Engineering, IEEE Transactions on*, 53(8):1594–1604, 2006.

[11] S. Gabriel, R.W. Lau, and C. Gabriel. The dielectric properties of biological tissues: II. Measurements in the frequency range 10 Hz to 20 GHz. *Physics in Medicine and Biology*, 41(11):2251–2269, 1996.

[12] B. Gustavsen and A. Semlyen. Rational approximation of frequency domain responses by vector fitting. *IEEE Transactions on Power Delivery*, 14(3):1052–1059, 1999.

[13] Matthias A Hein. Ultra-wideband radar sensors for biomedical diagnostics and imaging. In *Ultra-Wideband (ICUWB), 2012 IEEE International Conference on*, pages 486–490. IEEE, 2012.

[14] Marko Helbig, Ingrid Hilger, Martin Kmec, Gabriella Rimkus, and Jürgen Sachs. Experimental phantom trials for UWB breast cancer detection. In *Microwave Conference (GeMiC), 2012 The 7th German*, pages 1–4. IEEE, 2012.

[15] Ingrid Hilger, Christiane Geyer, Florian Thiel, Francesco Scotto di Clemente, Frank Seifert, Gabriella Rimkus, Jürgen Sachs, Katja Dahlke, Marko Helbig, Matthias Hein, et al. *UltraMEDIS-Ultra-Wideband Sensing in Medicine*. INTECH Open Access Publisher, 2013.

[16] Walter Allan Kester. *Data conversion handbook*. Newnes, 2005.

[17] A. Kheirdoost, G. Moradi, E. Elkholy, A. Abdipour, and A.E. Fathy. Modeling and jitter improvement of SRD-based ultra-wideband pulse generator. *IEEE Transactions on Microwave Theory and Techniques*, 62(8):1736–1747, 2014.

[18] M. Klemm, D. Gibbins, J. Leendertz, T. Horseman, A.W. Preece, R. Benjamin, and I.J. Craddock. Development and testing of a 60-element UWB conformal array for breast cancer imaging. In *Antennas and Propagation (EUCAP), Proceedings of the 5th European Conference on*, pages 3077–3079, April 2011.

[19] Maciej Klemm, Ian Craddock, Jack Leendertz, Alan Preece, and Ralph Benjamin. Experimental and clinical results of breast cancer detection using UWB microwave radar. In *Antennas and Propagation Society International Symposium, 2008. AP-S 2008. IEEE*, pages 1–4. IEEE, 2008.

[20] Herbert Knapp, Martin Wurzer, Werner Perndl, Klaus Aufinger, Josef Bock, and Thomas F Meister. 100-Gb/s 2 7-1 and 54-Gb/s 2 11-1 PRBS generators in SiGe bipolar technology. *Solid-State Circuits, IEEE Journal of*, 40(10):2118–2125, 2005.

[21] Silicon Labs. *AN687: A primer on jitter, jitter measurement and phase-locked loops*. Silicon Laboratories, 2012.

[22] Benjamin Laemmle, Benjamin Sewiolo, and Robert Weigel. A m=9 up to 25Gb/s M-sequence generator IC for UWB radar applications in a low-cost SiGe BiCMOS technology. In *German Microwave Conference, 2009*, pages 1–4. IEEE, 2009.

[23] Michael Löhning and Gerhard Fettweis. The effects of aperture jitter and clock jitter in wideband ADCs. *Computer Standards & Interfaces*, 29(1):11–18, 2007.

[24] Paul M Meaney, Margaret W Fanning, Timothy Raynolds, Colleen J Fox, Qianqian Fang, Christine A Kogel, Steven P Poplack, and Keith D Paulsen. Initial clinical experience with microwave breast imaging in women with normal mammography. *Academic radiology*, 14(2):207–218, 2007.

[25] Natalia K Nikolova. Microwave imaging for breast cancer. *Microwave Magazine, IEEE*, 12(7):78–94, 2011.

[26] M. Persson, A. Fhager, H.D. Trefna, Y. Yu, T. McKelvey, G. Pegenius, J.-E. Karlsson, and M. Elam. Microwave-based stroke diagnosis making global prehospital thrombolytic treatment possible. *IEEE Transactions on Biomedical Engineering*, 61(11):2806–2817, 2014.

[27] M Roßberg, J Sachs, P Rauschenbach, P Peyerl, K Pressel, W Winkler, and D Knoll. 11 GHz SiGe circuits for ultra wideband radar. In *Bipolar/BiCMOS Circuits and Technology Meeting*, pages 70–73, 2000.

[28] J Sachs, M Kmec, R Herrmann, M Helbig, and K Schilling. Integrated pseudo-noise device with network analyzer performance for uwb sensing and component test. In *Signals, Systems, and Electronics (ISSSE), 2012 International Symposium on*, pages 1–6. IEEE, 2012.

[29] Jürgen Sachs, Peter Peyerl, and Rudolf Zetik. Stimulation of UWB-sensors: pulse or maximum sequence? In *International Workshop on UWB Systems, Oulu, Finland*, page 5, 2003.

[30] Benjamin Sewiolo, Benjamin Laemmle, and Robert Weigel. Ultra-wideband transmitters based on m-sequences for high resolution radar and sensing applications. In *Ph. D. Research in Microelectronics and Electronics*, pages 1–4. IEEE, 2010.

[31] T Michael Souders, Donald R Flach, Charles Hagwood, and Grace L Yang. The effects of timing jitter in sampling systems. *Instrumentation and Measurement, IEEE Transactions on*, 39(1):80–85, 1990.

[32] Tektronix. *Arbitrary Waveform Generator:AWG7102, AWG7101, AWG7052, AWG7051 Data Sheet*. Tektronix, 2019.

[33] Zaid J Towfic and Ali H Sayed. Clock jitter estimation in noise. In *Circuits and Systems (ISCAS), 2011 IEEE International Symposium on*, pages 1251–1254. IEEE, 2011.

[34] André Vander Vorst, Arye Rosen, and Youji Kotsuka. *RF/Microwave interaction with biological tissues*, volume 181. John Wiley & Sons, 2006.

[35] Sertac Yilmaz and Ibrahim Tekin. Ultra-wideband n-bit digitally tunable pulse generator. In *Ultra-Wideband, 2005. ICU 2005. 2005 IEEE International Conference on*, pages 438–441. IEEE, 2005.

[36] R.X. Zeng and J.H. Sinsky. Modified rational function modeling technique for high speed circuits. *IEEE MTT-S International Microwave Symposium Digest*, pages 1951–1954, 2006.

[37] X. Zeng, A. Fhager, Z. He, M. Persson, P. Linner, and H. Zirath. Development of a time domain microwave system for medical diagnostics. *IEEE Transactions on Instrumentation and Measurement*, 63(12):2931–2939, 2014.

[38] Cemin Zhang and Aly E Fathy. Reconfigurable pico-pulse generator for UWB applications. In *Microwave Symposium Digest, 2006. IEEE MTT-S International*, pages 407–410. IEEE, 2006.

A

Equivalent-time sampling

A.1 Avoiding spectral leakage

If one sample is recorded every period, the measurement time for capturing a single period is

$$T_{meas} = N_s T_s \tag{A.1}$$

This rectangular windowing of an infinitely long periodic signal in the time domain becomes a convolution with the function

$$S(f) = N_s T_s \cdot \mathrm{sinc}(f N_s T_s) \tag{A.2}$$

which is zero for $f = \pm k/(N_s T_s), k = 1, 2, 3, ...$ The Dirac delta functions with which $S(f)$ is convoluted are separated by

$$\triangle f = f_{rep} - f_s = \frac{T_s - L}{L T_s} = \frac{T_{eq}}{L T_s} \tag{A.3}$$

It is therefore of interest to know the leakage of the energy of one impulse onto neighbours by calculating

$$S(k\triangle f) = N_s T_s \cdot \mathrm{sinc}(k \triangle f N_s T_s) \tag{A.4}$$

Spectral leakage is therefore avoided if $\triangle f N_s T_s = 1$, or

$$f_{eq} = N_s f_{rep} \tag{A.5}$$

But since N_s is the number of samples per recorded period, it must take on positive integer values. The equivalent sampling rate f_{eq} is therefore restricted to integer multiples of the repetition rate f_{rep}.

A.2 Preservation of phase

Let the first sample of a period occur at $t = nN_sT_s + \phi$ where $n = 0, 1, 2, 3...$ and ϕ is a constant phase offset. Also, let the signal to be sampled be represented by the Fourier series

$$x_s(t) = \frac{a_0}{2} + \sum_{k=1}^{\infty} [a_k \cos(2\pi k f_{rep} t) + b_k \sin(2\pi k f_{rep} t)] \tag{A.6}$$

The sampled value at the start of the period is then

$$x_s(nN_sT_s + \phi) = \frac{a_0}{2} + \sum_{k=1}^{\infty}[a_k\cos(2\pi k f_{rep} nN_sT_s + 2\pi k f_{rep}\phi) \tag{A.7}$$

$$+b_k\sin(2\pi k f_{rep} nN_sT_s + 2\pi k f_{rep}\phi)] \tag{A.8}$$

But if we enforce the relationship $f_{eq} = N_s f_{rep}$ then we can make the substitution $N_sT_s = N_pL$, giving

$$x_s(nN_sT_s + \phi) = x_s(nN_pL + \phi) \tag{A.9}$$

$$= \frac{a_0}{2} + \sum_{k=1}^{\infty}[a_k\cos(2\pi k f_{rep}\phi) + b_k\sin(2\pi k f_{rep}\phi)] \tag{A.10}$$

$$= C \tag{A.11}$$

where C is a constant. This implies that the measurement starts at the exact same phase every time a new measurement is made.

B

Time domain simulations using S-Parameters

The most common way of characterizing a microwave system is by using S-Parameters because they are easily measured using a vector network analyser (VNA) and they are easily interpreted. They are however not well suited to time domain simulations because measurements are not performed over an infinite frequency range, leading to causality violations after taking the inverse Fourier transform. This problem can be avoided if the missing frequency data is filled in by fitting a rational model to the S-Parameter data [36]:

$$F(s) = \sum_{j=1}^{N} \left(\frac{c_j}{s - a_j} + d \right) e^{-s \cdot t_d} \tag{B.1}$$

where N is the number of poles, c_j and a_j are zeros and poles respectively, d is the direct feed term and t_d is the time delay. The vector fitting algorithm used for determining these parameters is discussed in [12]. The model in (B.1) can be expressed in state space form:

$$\begin{aligned} \dot{x}(t) &= Ax(t) + Bu(t) \\ y(t - t_d) &= Cx(t) + Du(t) \end{aligned} \tag{B.2}$$

where

$$A = \begin{bmatrix} a_1 & 0 & \cdots & 0 \\ 0 & a_2 & & \vdots \\ \vdots & & \ddots & 0 \\ 0 & \cdots & 0 & a_N \end{bmatrix}, B = \begin{bmatrix} 1 \\ \vdots \\ 1 \end{bmatrix}, C = \begin{bmatrix} c_1 & \cdots & c_N \end{bmatrix}, D = [d] \tag{B.3}$$

This method of performing time domain simulations using measured S-Parameters can easily be done in Matlab using the function `rationalfit` to fit the data to the rational model in (B.1) and `timeresp` to perform the time domain simulations given by (B.2).